



# DNA-loop-extruding SMC complexes can traverse one another in vivo

Hugo B. Brandão<sup>ID 1,4</sup>, Zhongqing Ren<sup>2,4</sup>, Xheni Karabojć<sup>2</sup>, Leonid A. Mirny<sup>ID 1,3</sup>✉ and Xindan Wang<sup>ID 2</sup>✉

**Chromosome organization mediated by structural maintenance of chromosomes (SMC) complexes is vital in many organisms. SMC complexes act as motors that extrude DNA loops, but it remains unclear what happens when multiple complexes encounter one another on the same DNA in living cells and how these interactions may help to organize an active genome. We therefore created a crash-course track system to study SMC complex encounters *in vivo* by engineering defined SMC loading sites in the *Bacillus subtilis* chromosome. Chromosome conformation capture (Hi-C) analyses of over 20 engineered strains show an amazing variety of chromosome folding patterns. Through three-dimensional polymer simulations and theory, we determine that these patterns require SMC complexes to bypass each other *in vivo*, as recently seen in an *in vitro* study. We posit that the bypassing activity enables SMC complexes to avoid traffic jams while spatially organizing the genome.**

Chromosomes from all kingdoms of life are actively maintained and spatially organized to ensure cell viability. Structural maintenance of chromosomes (SMC) complexes play a key role in spatially organizing chromosomes and function in many processes, including chromatin compaction, sister-chromatid cohesion, DNA break repair and regulation of the interphase genome<sup>1,2</sup>. Although their importance has been recognized for over 25 years, evidence for a molecular mechanism for how SMC complexes function has only recently emerged. Recent single-molecule experiments and chromosome conformation capture (Hi-C) studies have shown that the condensin and cohesin SMC complexes can translocate on DNA and extrude DNA loops at rates of ~1 kb s<sup>-1</sup> (refs. <sup>3–11</sup>). The process of DNA loop extrusion by SMC complexes is emerging as a universal mechanism by which these proteins organize the three-dimensional (3D) genome in eukaryotes and prokaryotes<sup>2</sup>. It remains unclear, however, what happens in a living cell when multiple SMC complexes encounter one another<sup>12</sup>. Understanding the outcome of such encounters is fundamental to elucidating how chromosomes are spatially organized by the process of DNA loop extrusion.

Encounters between SMC complexes are expected to occur frequently in a cell. In eukaryotes, the cohesin and condensin SMC complexes are loaded at multiple chromosomal loci, at estimated densities between about 1 per 200 kb and 1 per 40 kb, and extrude loops of hundreds of kilobases (reviewed in ref. <sup>13</sup>). In many bacteria, SMC complexes are loaded by the protein ParB primarily at centromeric sequences called *parS* sites<sup>14–18</sup>. These sites often exist in multiple copies close to one another<sup>19</sup>. In bacteria without the ParB/*parS* system, such as *Escherichia coli*, the SMC-like MukBEF complex loads non-specifically, but creates long DNA loops<sup>20,21</sup>. Therefore, in both eukaryotes and bacteria, SMC complexes will frequently encounter others when extruding DNA loops. Most efforts toward understanding the chromosome organizing capacity of SMC loop extruders have assumed that translocating complexes are impenetrable to each other<sup>22</sup> (also reviewed in refs. <sup>2,12</sup>). A recent single-molecule study using *Saccharomyces cerevisiae* condensins

challenged this assumption and demonstrated that condensins can traverse past each other *in vitro*<sup>23</sup>. How SMC complexes interact *in vivo* (that is, traversing, blocking or unloading each other, and so on) and the implications of these interactions for chromosome folding remain unknown. In this Article, we show that *Bacillus subtilis* SMC complexes can traverse past each other *in vivo* in a quantitatively predictable manner, resulting in an unexpected diversity of chromosome folding structures.

## Results

**Engineering an *in vivo* system for SMC complex encounters.** We set up an SMC complex ‘crash-course track’ system to probe the effects of encounters between loop-extruding factors (LEFs, Fig. 1a). We engineered *B. subtilis* strains to contain one, two or three *parS* sites, and we varied the relative separations and positions of the SMC loading sites (Figs. 1b and 3a,b). This allowed us to better resolve the effects of encounters between SMCs than in the wild-type system, which has nine *parS* sites in proximity to one another<sup>24–26</sup>. Moreover, to remove potential confounding effects of interactions between the replication machinery and SMCs, and to eliminate potential interactions between sister chromatids, we synchronized cells in G1 phase by expressing the protein SirA. SirA inhibits replication initiation while allowing ongoing rounds of replication to complete, leaving cells with single chromosomes<sup>27</sup>. We then investigated chromosome interaction patterns using Hi-C and protein distributions by chromatin immunoprecipitation (ChIP-seq) assays<sup>10,26,28</sup>.

**SMCs translocating toward one another slow each other down.** Consistent with our previous findings, strains containing single SMC loading sites at -94° or -59° (that is, genome positions of 2,981 kb or 3,377 kb out of 4,033 kb, Extended Data Fig. 1a) displayed DNA juxtaposition, or ‘lines’ on the Hi-C map, indicative of large tracks of DNA being brought together in a hairpin-like structure (Fig. 1c, left and center panels)<sup>10,29</sup>. In striking contrast, a strain with both of these *parS* sites exhibited a complex star-shaped pattern (Fig. 1c, right). This pattern has additional features that are

<sup>1</sup>Graduate Program in Biophysics, Harvard University, Cambridge, MA, USA. <sup>2</sup>Department of Biology, Indiana University, Bloomington, IN, USA. <sup>3</sup>Institute for Medical Engineering and Science, Massachusetts Institute of Technology, Cambridge, MA, USA. <sup>4</sup>These authors contributed equally: Hugo B. Brandão, Zhongqing Ren. ✉e-mail: [leonid@mit.edu](mailto:leonid@mit.edu); [xindan@indiana.edu](mailto:xindan@indiana.edu)

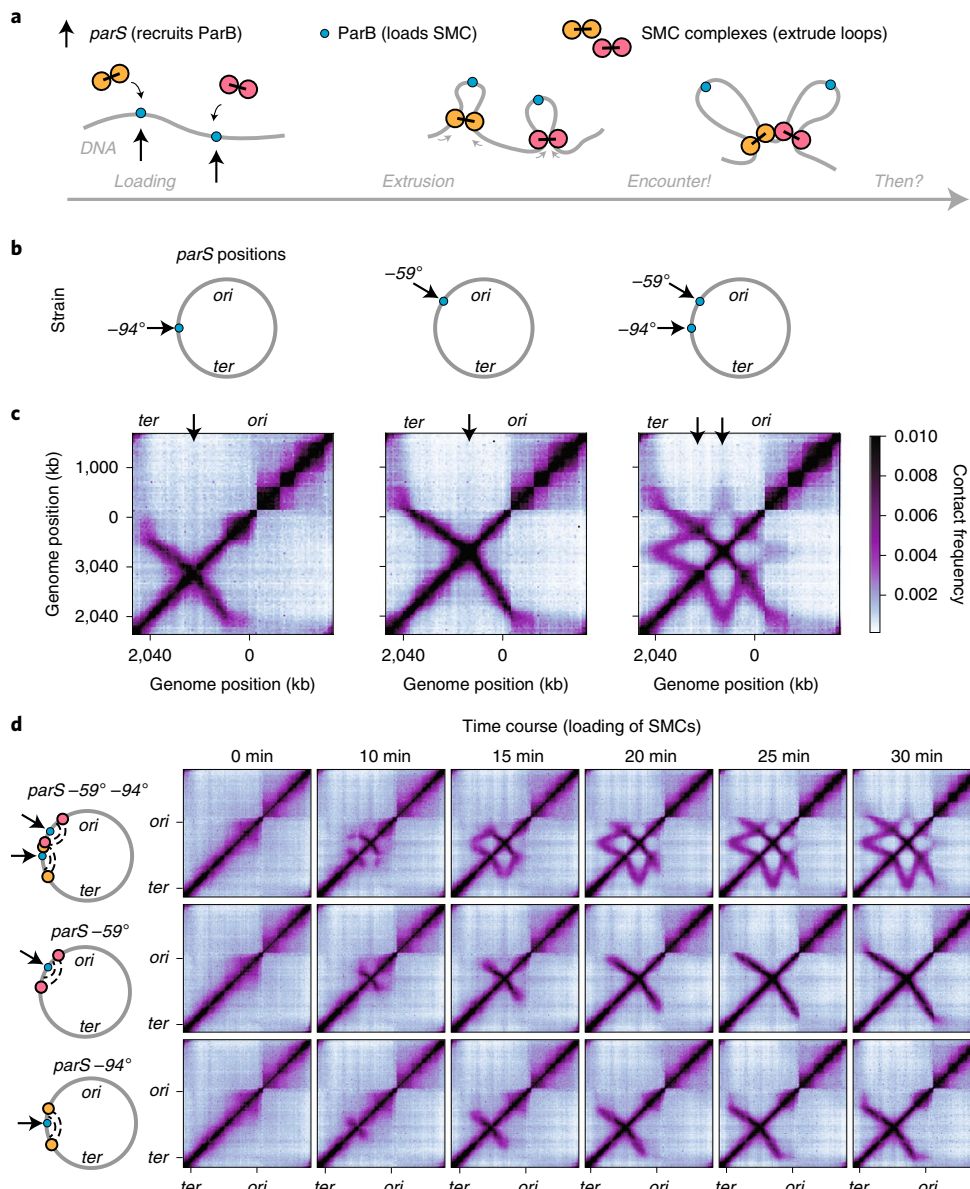


**Fig. 1 | Experimental system to study the effect of 'collisions' between SMC complexes.** **a**, Experimental set-up. **b**, Schematic of strains indicating the positions of single *parS* sites inserted on the chromosome of *B. subtilis*. **c**, Hi-C maps of G1-arrested cells. *B. subtilis* strains contain a single *parS* site at  $-94^\circ$  (2,981 kb, left),  $-59^\circ$  (3,377 kb, middle) or at both sites (right). **d**, Hi-C maps from a time-course experiment following induction of ParB, the SMC loading protein, for the indicated times. The schematic illustrates the paths of SMC loop extruders superimposed on the chromosome for each strain at 10 min following ParB induction.

absent from strains with single *parS* sites, indicating that non-trivial interactions occur between SMC complexes translocating from opposing sites. Hi-C performed for the same strains growing in asynchronous cultures revealed similar patterns, albeit less intense, showing that these patterns are not specific to G1 arrest (Extended Data Fig. 1b). To understand how the star-shaped pattern emerged, we performed a time-course Hi-C experiment in cells with an IPTG-inducible expression of the SMC loader, ParB, as the sole source of the ParB protein (Fig. 1d). We took samples in the absence of IPTG and at 5-min intervals after its addition. By tracking the juxtaposition of DNA flanking the *parS* site over time, we measured the rates of DNA loop extrusion. In the strains with a single *parS* site, the extrusion rate was  $\sim 0.8 \text{ kb s}^{-1}$  towards the replication terminus (*ter*) and  $\sim 0.6 \text{ kb s}^{-1}$  towards the replication origin (*ori*), similar to previous measurements<sup>10,29</sup>. By contrast, in the strain with

both *parS* sites, the extrusion rate in the section between the *parS* sites (that is, where SMC complexes move toward one another) was lower by a factor of  $\sim 1.2$ , but outside that section the rates remained unaltered (Extended Data Fig. 2a, Methods and Supplementary Notes 1–5). This slowdown is most evident from the change in the tilt of the lines when comparing to strains with single *parS* sites (Extended Data Fig. 2b,c). These results suggest that SMCs translocating toward one another can effectively slow each other down. We thus investigated how SMCs interact to create this slowdown and the complex chromosome folding patterns.

**Interactions between SMCs help explain contact patterns.** We first broke down the star-shaped Hi-C interaction pattern into different line segments and investigated how these lines may be explained by a process of DNA loop extrusion by SMC complexes (Fig. 2a).

Lines 1 and 2, similar to those seen in maps for strains with one *parS* site, can be formed by single SMC complexes (making ‘singlet contacts’) as they translocate away from their respective *parS* loading sites and juxtapose the flanking DNA. By contrast, lines 3, 4 and 5 are probably formed by interactions between SMC complexes, and in the following we provide a possible origin for these lines. Line 3 can emerge when two SMC complexes coming from different *parS* sites meet in between the *parS* sites. In addition to each of their singlet contacts (that is, on lines 1 and 2), they produce another contact by bridging DNA along their flanks (Fig. 2a,ii). Because SMC complexes in different cells can meet at different genome positions, the location of the additional contact varies. Thus, when averaged over a population of cells, the contacts mediated by SMC collisions (that is, ‘collision doublets’) result in line 3 (Fig. 2a,ii and Supplementary Fig. 1). Line 4 can emerge if the meeting point of the SMC complexes is at the *parS* site. For example, if one SMC complex from *parS* site S2 extrudes past site S1, and a second SMC complex loads at site S1 close to that moment, then the SMC complexes enter into a ‘nested-doublet’ configuration. As long as the two complexes continue to extrude DNA, they generate line 4 over time (Fig. 2a,iii). Finally, if the second SMC complex (loaded from S1) of the ‘nested-doublet’ configuration meets a third SMC complex (loaded from S2), then the different meeting points between three SMC complexes produce the contacts of line 5 (Fig. 2a,iv) in addition to lines 3 and 4. It is possible to envision an alternate mechanism for the formation of line 5 (and line 4) (S. Gruber, personal communication) (Supplementary Fig. 2), whereby ParB molecules form a ‘temporary loading site’ at a mirrored *parS1* location on the juxtaposed DNA; however, we can rule this out on theoretical grounds as well as experimentally (Supplementary Fig. 2). Thus, our line-based decomposition provides a framework for interpreting complex Hi-C patterns as assemblies of SMC complexes and describes a possible series of events leading to each of the lines of the star-shaped pattern.

**Polymer simulations rule out certain mechanisms of pattern formation.** Next, we used polymer simulations to understand how the patterns observed by Hi-C emerge from the rules of engagement between SMC complexes. In our simulations, each LEF was represented by two connected motor subunits<sup>29–31</sup> (Fig. 2a). By translocating away from their loading site, the connected motors bring genomic loci into spatial proximity. Based on previous studies of the *B. subtilis* SMC complex<sup>32</sup>, we allowed loop extruders to load anywhere on the genome, but with a preferential bias (see below) such that most loaded at *parS* sites. Because previous studies showed that two motor activities of the same LEF are independent of each other, we allowed continued extrusion by a motor subunit, even if the other subunit’s translocation was blocked<sup>9,10,29</sup>. From the simulations of loop extrusion on a 3D polymer, we then created Hi-C-like contact maps<sup>30,31</sup> (Supplementary Notes 1–5 provide all simulation details).

Our attention turned to three main rules of interaction between SMC complexes: blocking, unloading or bypassing (Fig. 2b and Supplementary Fig. 1). We also explored various other models, including 3D interactions between extruders, the effect of sticky DNA, the effect of extruder subunits reversing direction after collision, among others (Supplementary Figs. 2 and 3). However, we ruled out these other models due to their inability to create lines 4 and 5 or because they generated lines not observed experimentally (Supplementary Figs. 2 and 3).

Similar to previous work, we first considered models involving only blocking<sup>13,22,30</sup>, then extended the model to include a facilitated unloading of blocked SMC complexes. We allowed collided motor subunits to pause (in the blocked state) before unloading with a specified rate. By sweeping over a broad range of unloading rates and SMC complex numbers, we found that it was not possible to reproduce lines 4 and 5 at intensities seen on experimental Hi-C maps (Extended Data Fig. 3). The failure of this class of models in reproducing lines 4 and 5 is due to an inability to efficiently form nested configurations. For example, with few SMC complexes per chromosome, it is easy for an SMC complex loaded at *parS* site S2 to reach *parS* site S1. However, a small loading rate due to few SMC complexes makes it unlikely that a second SMC complex will bind to S1 at the moment the S2 SMC complex extrudes past it. With high numbers of SMC complexes, the loading rate at each *parS* site is larger. However, traffic jams due to SMC collisions between the S1 and S2 sites prevent most SMCs from ever reaching the opposing site. Therefore, the blocking and unloading model results in low numbers of nested-doublet configurations and cannot create lines 4 and 5 at the intensities observed experimentally (Supplementary Note 5).

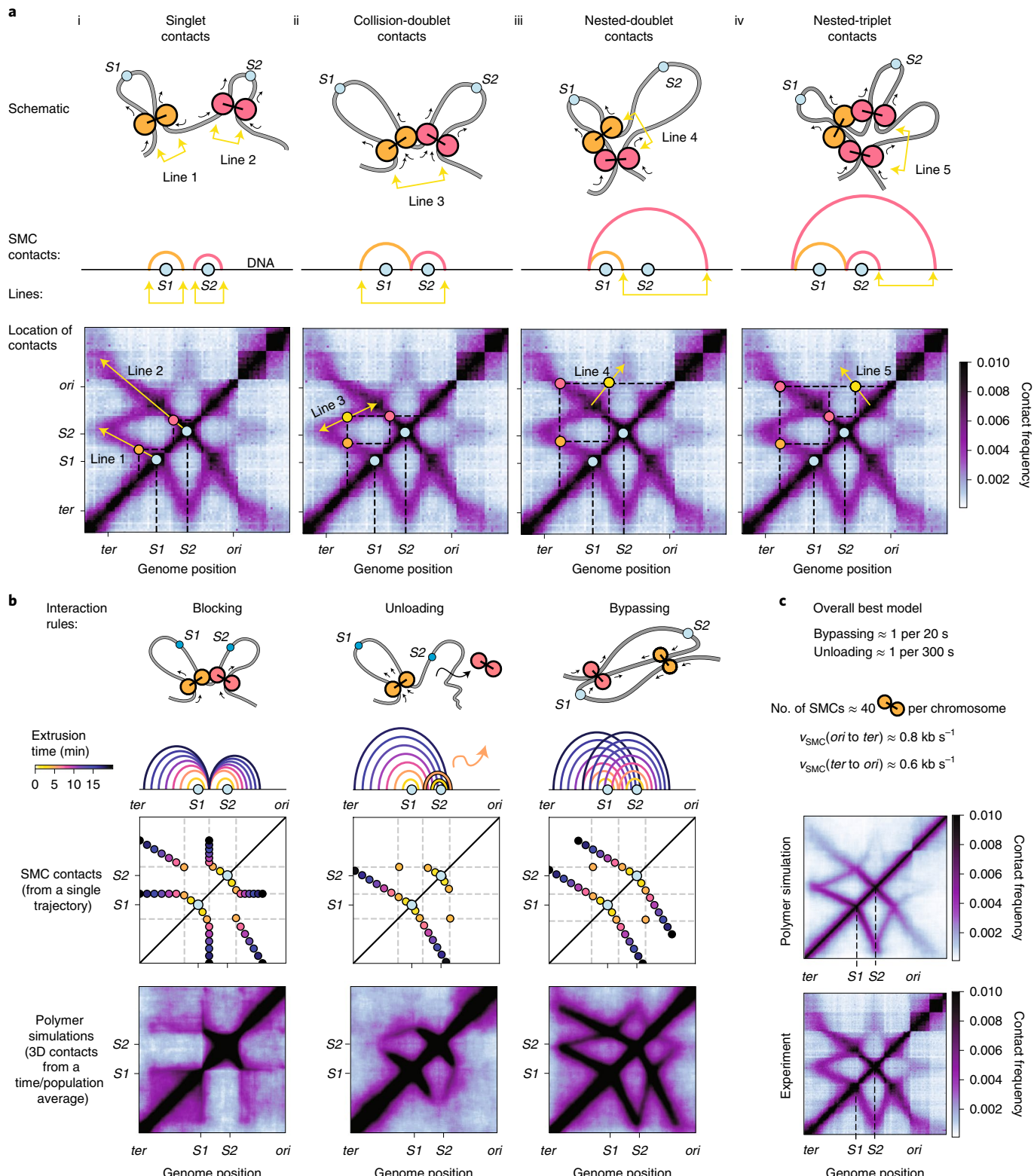
**A model of SMC complexes bypassing each other explains experimental data.** We extended the blocking-only model by allowing SMC complexes to bypass one another, which was also motivated by recent single-molecule experiments<sup>23</sup>. In this blocking and bypassing model, we assumed that, when two SMCs meet, the collided subunits pause but can traverse each other with some specified rate. However, we did not allow facilitated unloading. Strikingly, the blocking and bypassing model was sufficient to robustly reproduce the star-shaped Hi-C pattern (Fig. 2b and Extended Data Fig. 4a). Moreover, this blocking and bypassing model produced the observed ‘tilting’ of lines 1 and 2 away from each other for certain bypassing rate and SMC number combinations (Extended Data Fig. 4b). Nevertheless, the bypassing mechanism by itself generated lines 4 and 5 more intensely than observed experimentally, suggesting that too many SMC complexes were entering nested configurations (Fig. 2a). We thus added back the facilitated unloading assumption to the blocking and bypassing model. This allowed us to tune the relative intensities of lines 3, 4 and 5 and obtain Hi-C maps that looked strikingly similar to the experimental data (Extended

**Fig. 2 | Specific interactions between SMC complexes leave unique Hi-C signatures.** **a**, Decomposition of the Hi-C map into assemblies of SMC complexes. The schematic diagram (top row) and the arch-diagram representation (middle row) of the SMC assemblies are superimposed on a Hi-C map (bottom row). Locations of point-like SMC-mediated contacts are depicted either by a yellow arrow (top, middle), or by a yellow/pink dot on the Hi-C map (bottom). S1 and S2 are SMC loading sites (blue dots). SMCs loaded on S1 are orange and on S2 are pink. These colors are consistent between rows to facilitate comparison. SMC complexes in different cells can meet at different genome positions. When averaged over a population of cells, the contacts mediated by SMC collisions generate ‘lines’ in the Hi-C map. **b**, Possible interaction rules of SMC complexes (blocking, unloading, bypassing). The schematic (top row) illustrates the interaction. The arch diagram (second row) captures the 1D contact along the DNA. The 2D Hi-C-like contact trace (third row) captures the spatio-temporal behavior of a single interaction by a pair of extrusion complexes. For the second and third rows, extrusion time is shown over a 15-min period, and times are indicated by arch or dot colors. A 3D polymer simulation and the resulting contact map for each interaction rule are shown on the bottom row. A broader parameter sweep is provided in Extended Data Figs. 3–5. **c**, A parameter sweep over the three interaction rules accounting for different rates gives a best-match model (Supplementary Figs. 4–7 and Methods). For  $n=40$  extrusion complexes per chromosome, we find that bypassing rates are ~1 per 20 s and unloading rates are ~1 per 300 s. A comparison between the experimental data and a 3D polymer simulation of the model is shown.

Data Fig. 5). Of all the models that were tested, the combined bypassing and unloading model was the only one that produced all lines 1–5 at the same time, with the observed relative intensities.

The resulting integrated model included the rules for SMC encounters (that is, blocking, bypassing and facilitated unloading), as well as the rules for basal SMC dynamics, and totaled six parameters: the bypassing rate, the facilitated unloading rate, the number of SMC complexes per chromosome, the SMC loading

rates at *parS* sites versus other sites and the spontaneous dissociation rate of SMCs in the absence of collisions (Supplementary Notes 1–5). Uniquely, we found that we could fix all six model parameters experimentally using a combination of Hi-C, ChIP-seq data and theoretical constraints between parameters (Methods), finding a unique region of parameter space that best fit all of the available data (Supplementary Figs. 4–7 and Supplementary Notes 1–5).



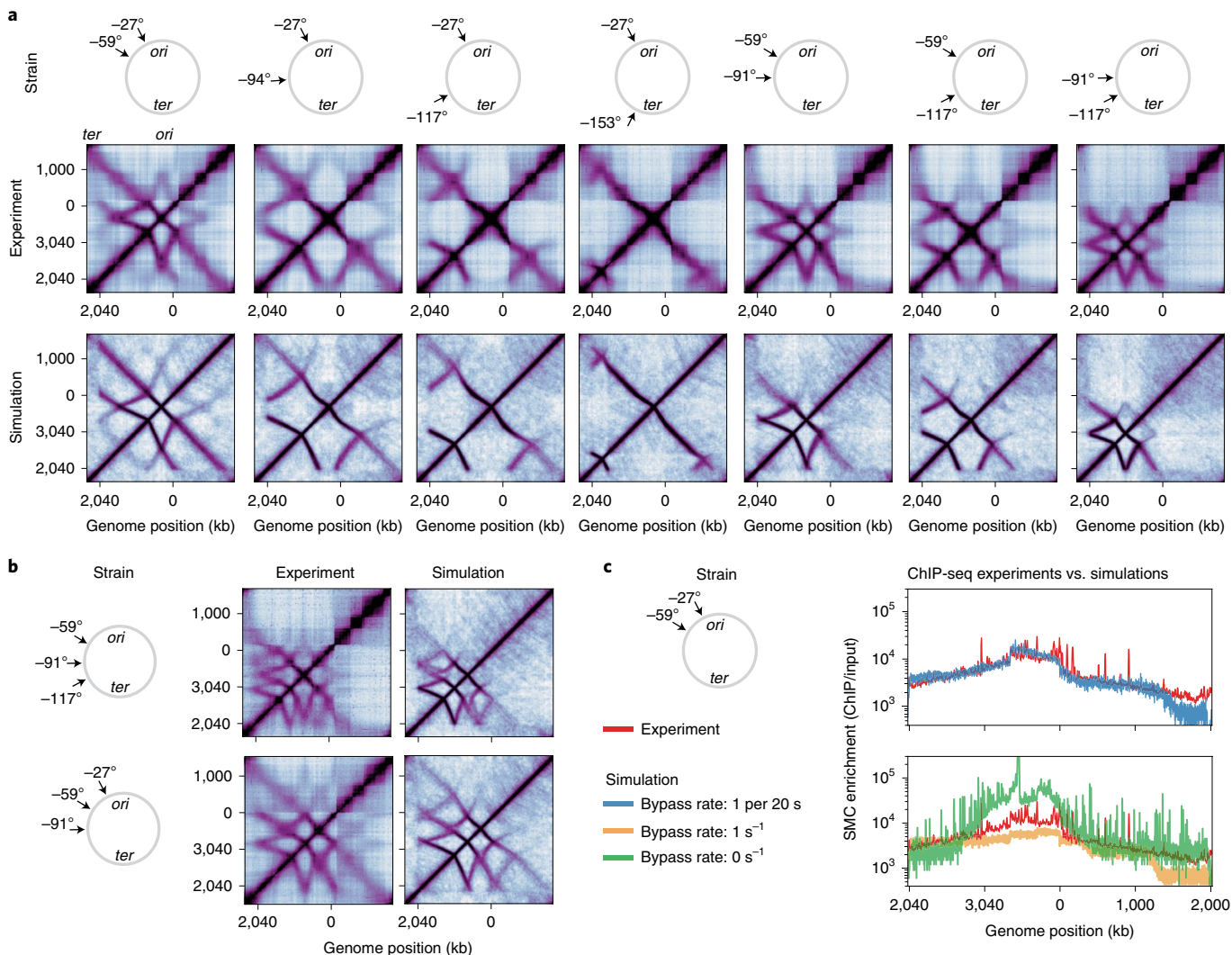


**Fig. 3 | Validating and testing a model of in vivo Z-loop formation.** **a,b**, Data and simulations of Hi-C maps of strains containing two *parS* sites (**a**) or three *parS* sites (**b**). All models use the same parameters as identified in Fig. 2c. **c**, A comparison of SMC occupancy between experimental ChIP-seq (red) and our model for different rates of bypassing (blue, green and yellow). Notably, a bypassing rate of ~1 per 20 s identifies the best-fit model. This comparison is independent of the comparisons between Hi-C results and modeling.

In the best models, there were 25–45 SMC complexes present on each chromosome after 1 h of G1 arrest. SMCs paused for ~20 s when they met each other, before either bypassing or unloading from the chromosome (Fig. 2c). These momentary pauses upon SMC collisions can explain the overall observed ‘slowdown’ of SMC complexes discussed earlier. Moreover, we found that bypassing was ~10–20 times more likely to occur than unloading (the bypassing rate was ~0.03–0.1 s<sup>-1</sup> and the unloading rate was ~0.002–0.005 s<sup>-1</sup>). Thus, the bypassing mode of conflict resolution dominated over unloading and was essential for explaining the observed lines on the Hi-C map mediated by SMC complex dynamics. Fixing the rates for bypassing at 0.05 s<sup>-1</sup> and unloading at 0.003 s<sup>-1</sup>, and with 40 extruders per chromosome, polymer simulations quantitatively reproduced the SMC-mediated lines 1–5 seen in the experimental Hi-C data (Fig. 2c), and raised the possibility of predicting chromosome folding in other engineered strains.

**A model of SMC complexes bypassing each other predicts new patterns.** We thus investigated whether the bypassing and unloading rules were generally applicable to SMC encounters. We generated seven other strains containing two *parS* sites at various locations

and two strains containing three *parS* sites, then performed Hi-C in G1-arrested cells (Fig. 3a,b) and exponentially growing cells (Extended Data Fig. 6). These engineered strains produced an impressive diversity of Hi-C contact patterns, which depended on the relative spacing and positioning of SMC loading sites. Nevertheless, all the complex multi-layered interaction features could be understood via the descriptions of SMC-mediated contacts (Fig. 2a). Strikingly, using the same parameter values as above (that is, from Fig. 2c), the model of SMC bypassing and unloading reproduced all the emergent Hi-C contact features away from the primary diagonal, showing strong agreement in all nine strains (Fig. 3a,b). We note that in the experimental Hi-C maps, chromosomal interaction domains (CIDs) on the primary diagonal are evident in all of our strains (Figs. 2c and 3a,b). These CIDs are also present in a strain without *parS* sites (Supplementary Fig. 5), suggesting that they are loci-specific and are not related to specific loading of SMC complexes at *parS* sites. We did not add these locus-specific assumptions to reproduce these CIDs in our simulations.

As an independent way of investigating the consequences of SMC encounters, we determined the SMC distributions by performing ChIP-seq and compared the experiments to our model

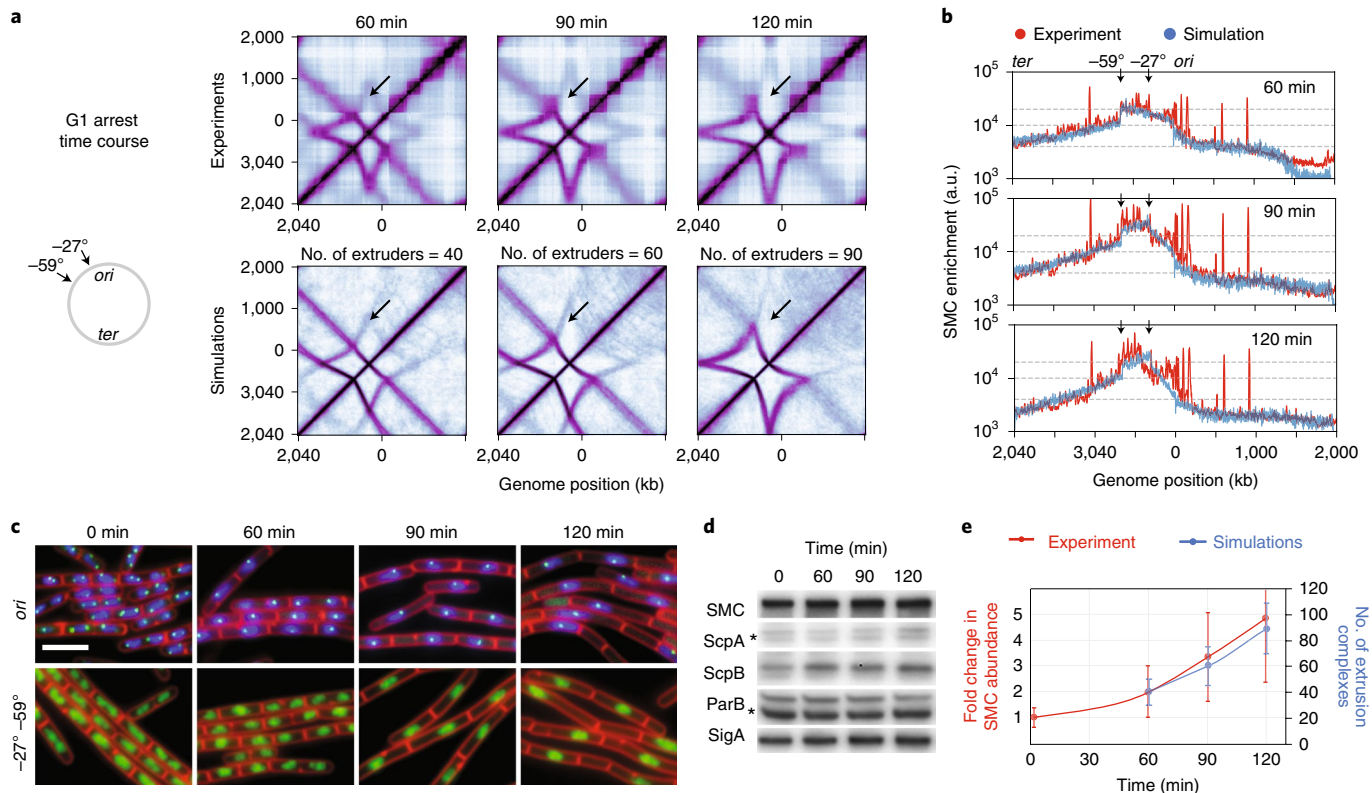


**Fig. 4 | The number of SMC complexes per chromosome tunes the shape of contact maps.** **a,b**, A time course of Hi-C (**a**) and SMC ChIP-seq (**b**) tracking chromosome structure changes and SMC occupancy following replication arrest by SirA. Experiments are compared to simulations in which the numbers of SMC complexes per chromosome are increased, but all other simulation parameters are kept as determined in Fig. 2c. **c**, Top row: fluorescence microscopy of tagged chromosome loci marking the *ori* (green) and the DAPI-stained nucleoid (blue). Bottom row: nucleoids in a strain containing  $-27^\circ$  and  $-59^\circ$  *parS* sites. Membranes are stained in red. This experiment was independently performed twice with similar results. Scale bar, 4  $\mu$ m. Quantification of the data is provided in Extended Data Fig. 8b. **d**, Western blots for the indicated proteins. The asterisks indicate the correct bands. **e**, Quantification of the number of extrusion complexes per chromosome (assuming extrusion complexes are dimers of SMC complexes). The numbers are calculated using fluorescence microscopy, western blot and whole-genome sequencing data quantifications. For simulations, confidence intervals are estimated by qualitatively matching simulated contact maps (that is, the size of the star shape, angles and the intensities of lines 1–5) to experimental Hi-C maps. Means and standard deviations are shown for the experimental fold change in SMC abundance values. The numbers of cells analyzed were  $n=725, 580, 702$  and  $557$  for the four time points. See also Extended Data Fig. 8. Unprocessed images for **c** and full scans of the blots in **d** are uploaded to Mendeley Data (<https://doi.org/10.17632/vgw8sjxsvy.1>).

predictions (Fig. 3c). We found that a bypassing rate of ~1 per 20 s was necessary for quantitative agreement between experiments and simulations (Fig. 3c). With the bypassing rate too low, SMCs tended to accumulate strongly near the loading sites, and with the bypassing rate too high, the occupancy profile was too flat. This rate of bypassing (~1 per 20 s) obtained by modeling of ChIP-seq is in strong agreement with the value inferred from modeling of Hi-C data. We note that our models work well to capture the genome-wide trends of SMC occupancy except near the terminus region, indicating that our understanding of the SMC loading at *parS* sites and interaction rules is good, but future work needs to be done to elucidate how SMCs interact with the terminus. Together, the agreement of the model with both Hi-C and ChIP-seq lends strong support for the notion that SMC complexes can translocate past one another on DNA *in vivo* after short pauses.

**SMC traffic jams explain the time-dependent change of Hi-C patterns.** Having studied the effects of changing loading site positions and spacings, we next studied the effect of time on chromosome reorganization after G1 arrest. In wild-type cells, which harbor nine *parS* sites, the spatial chromosome organization changes dramatically; the most prominent feature of the Hi-C map (the central diagonal) vanishes after 2 h and is replaced by two smaller tilted

lines<sup>26</sup>. However, before examining the time-dependent changes in the wild-type system, we investigated the time course in a simplified system with one and two *parS* sites. Over a 2 h window, although no changes occurred to the Hi-C lines 1 or 2 with one *parS* site (Extended Data Fig. 7a), we observed major changes in strains with two sites (Fig. 4a and Extended Data Fig. 7b). Specifically, the star shape became progressively larger due to an increased tilt of lines 1 and 2 away from each other (Fig. 4a and Extended Data Fig. 7b). This indicated that the SMC translocation between the *parS* sites was further slowed over time and demonstrated that the observed changes were due to interactions of SMCs translocating from different *parS* sites. With simulations, we could also achieve a similar effect (Fig. 4a and Extended Data Fig. 4). By increasing the numbers of loop extruders present on the chromosome we obtained more frequent SMC collisions, which led to an overall slowing down of extrusion between *parS* sites and the larger star-shaped pattern. The numbers of loop extruders per chromosome necessary to recapitulate the Hi-C data were  $40 \pm 10$ ,  $60 \pm 15$  and  $90 \pm 20$  (Fig. 4a). Reassuringly, the numbers of extruders per chromosome that gave the best agreement with Hi-C also independently reproduced SMC ChIP-seq profiles for the specific time points (Fig. 4b). We thus hypothesized that continued protein synthesis after replication inhibition resulted in a higher number of SMC complexes per DNA molecule.

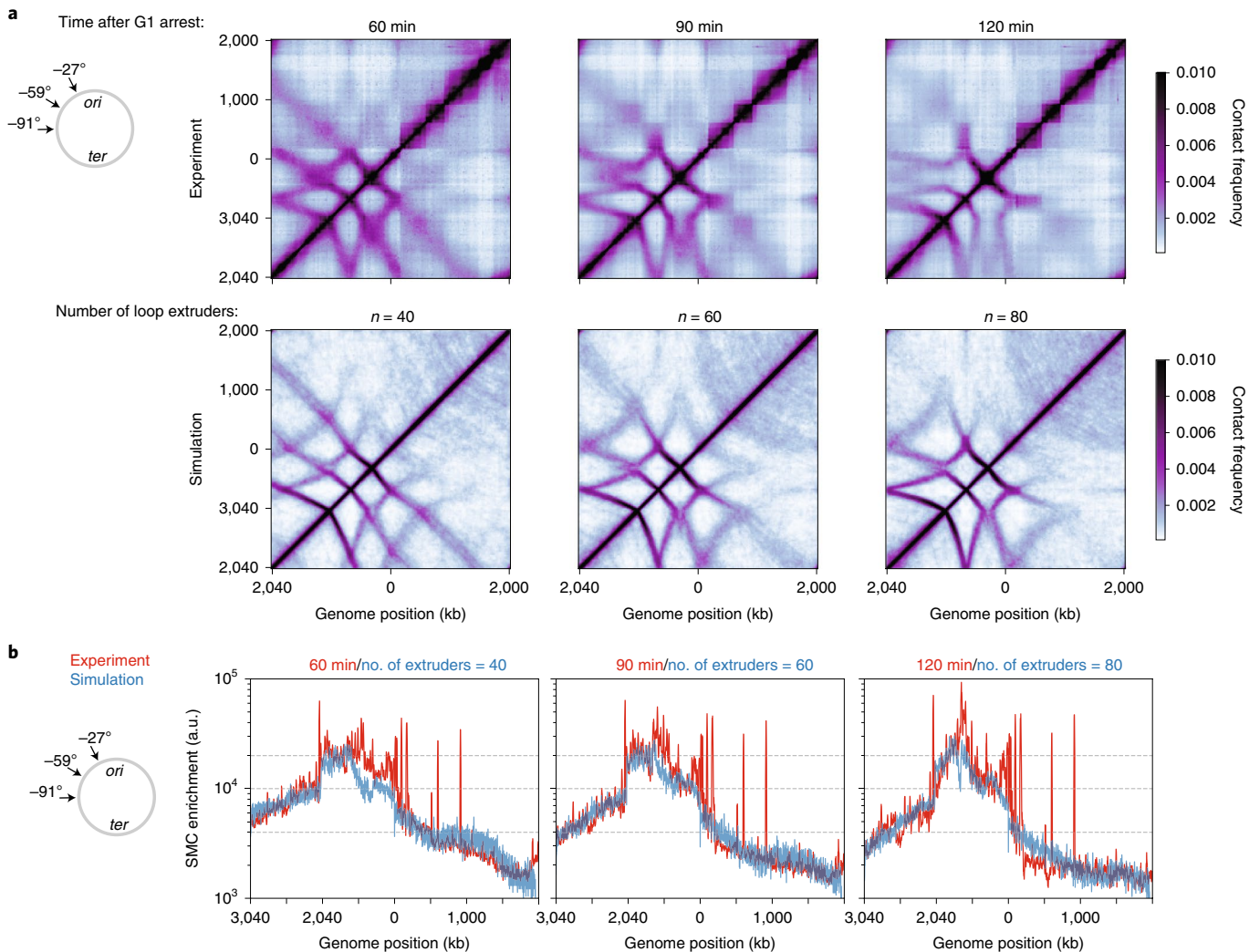


**Fig. 5 | Time-dependent change of Hi-C patterns in strains with three *parS* sites.** **a**, Hi-C time-course experiments upon SirA induction (top) and corresponding 3D polymer simulations (bottom) for a strain with three *parS* sites at positions  $-91^\circ$ ,  $-59^\circ$  and  $-27^\circ$ . **b**, Anti-SMC ChIP-seq performed for the same strains, in experiments (red) and simulations of SMC abundance (blue). In the simulations, the bypassing rate was  $0.05\text{ s}^{-1}$  and the facilitated dissociation rate was  $0.003\text{ s}^{-1}$  (that is, the same as in Fig. 4a).

To quantify the change in SMC abundance experimentally, we measured the chromosome copy numbers per cell and SMC complex abundances over time. Marker frequency analyses<sup>33</sup> by whole-genome sequencing and fluorescence microscopy showed that cells retained only one copy of the genome per cell for the duration of the experiment (Fig. 4c and Extended Data Fig. 8). Immunoblot analyses of cells growing under the same conditions showed that ParB and SMC complex subunit levels per unit cell mass remained constant over time (Fig. 4d). However, we found that at 90 min and 120 min after G1 arrest, the nucleated cells' length/mass increased to 1.7-fold and 2.4-fold the 60-min value (Fig. 4c and Extended Data Fig. 8). From the increased cell lengths and constant density of SMC subunits, we inferred the relative changes in SMC complex numbers per chromosome (Fig. 4e). These fold-change values in SMC complex numbers are in good agreement with the numbers of loop extruders independently identified by Hi-C and simulations above (Fig. 4e). Thus, continued protein synthesis after replication inhibition leads to increased numbers of SMC complexes per chromosome.

Next, we directly tested the role of SMC complex abundance on chromosomal organization by perturbation. We hypothesized that

overexpression of the SMC complex would lead to a faster evolution of the observed Hi-C patterns in a G1-arrest time course. Consistently, we observed this trend experimentally in a strain with two *parS* sites (Extended Data Fig. 9): at the 60-min mark, we saw the traces typical of 90 min in the absence of SMC overexpression. This confirms the role of SMC abundance in tuning chromosome spatial organization and the changing shapes of the Hi-C interaction patterns.

Finally, we studied the most complex systems—strains with three *parS* sites or nine *parS* sites (that is, wild-type cells)—and investigated the mystery of the vanishing ‘central’ lines. In these strains, the disappearance of the central line in Hi-C was accompanied by the accumulation of SMCs between the *parS* sites as seen in ChIP-seq (Figs. 5 and 6a). Despite the complexity of the changes over time, our model captured these effects (Figs. 5 and 6a) and helped to understand what was happening. Under normal growth conditions, with basal SMC levels, collisions between SMCs from adjacent *parS* sites are resolved by bypassing (in  $\sim 20\text{ s}$ ) before the next extrusion complex arrives. However, the increased number of SMCs makes the rate of new collisions higher than the rate of bypassing. This effect is particularly strong for the central sites, where extruders are jammed in from both sides. This finally results in effective

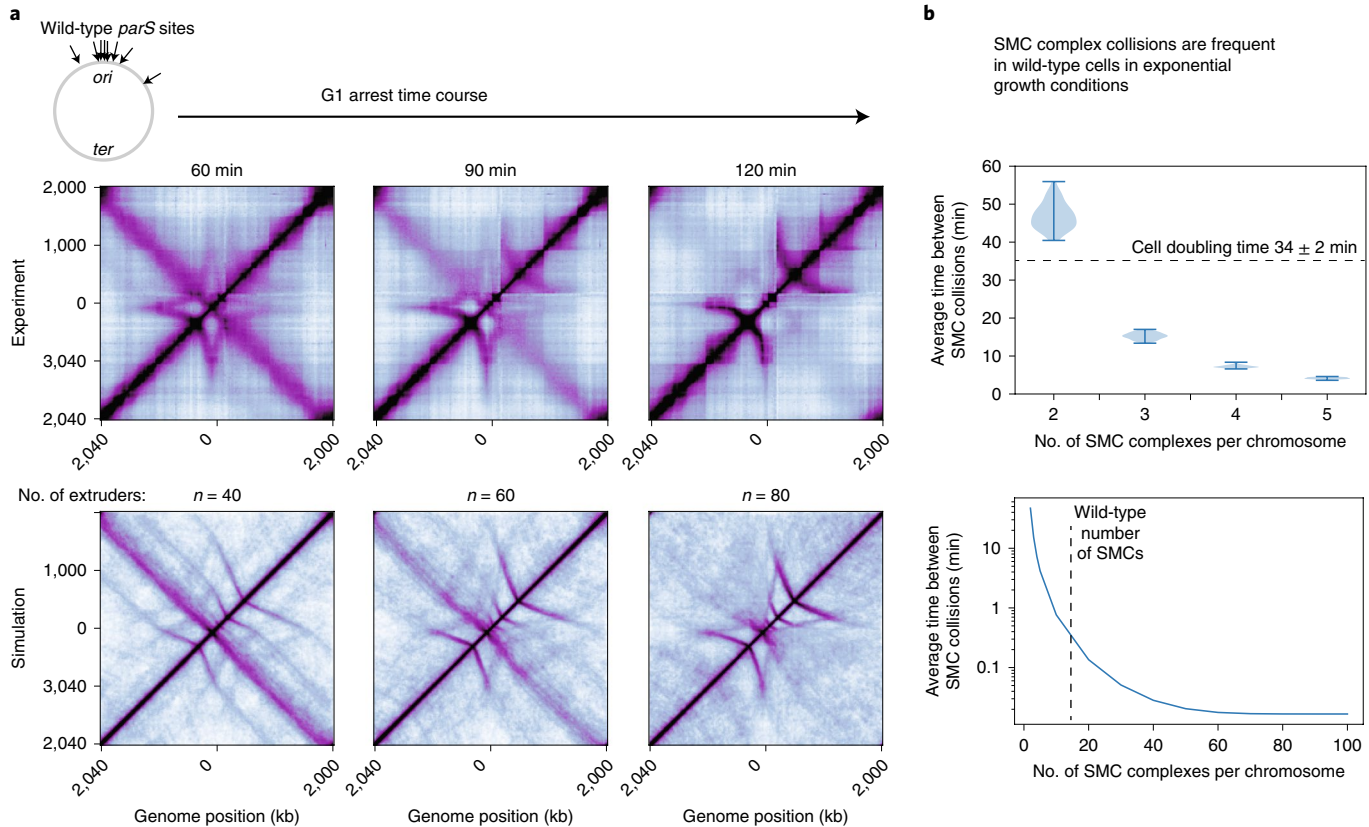


**Fig. 6 | Time-dependent change of Hi-C patterns in strains with wild-type *parS* sites.** **a**, Experiments (top) and simulations (bottom) of G1-arrested wild-type *B. subtilis* cells. The wild-type *parS* sites occur at positions  $-27^\circ$ ,  $-6^\circ$ ,  $-5^\circ$ ,  $-4^\circ$ ,  $-1^\circ$ ,  $+4^\circ$ ,  $+17^\circ$ ,  $+42^\circ$  and  $+91^\circ$ . In the simulation, we excluded the  $+91^\circ$  *parS* site because SMC complex loading is strongly attenuated by the proximal chromosome interaction domain boundary and SMC binding at this site is substantially weaker than at the others<sup>24</sup>. In both experiments and simulations, the central diagonal gradually vanishes due to traffic jams between extruders at the *ori*-proximal *parS* sites after increasing numbers of loop extruders. The bypassing rate was  $0.05\text{ s}^{-1}$  and the unloading rate was  $0.003\text{ s}^{-1}$  in the simulations. **b**, Calculated average time between SMC collision events from 61 independent simulations, where each simulation contains measurements of at least 150 collision events. Horizontal bars indicate the extrema of simulation values; even for cells with only five SMC complexes per chromosome, encounters are expected approximately every 10 min on every chromosome. For the expected number of SMC complexes in wild-type cells (black dashed line, bottom), the mean collision time is less than 1 min.

extrusion only from the outermost *parS* sites and gives rise to the disappearance of the central line (Figs. 5 and 6a). We conclude that bypassing plays an important role in preventing traffic jams between SMC complexes in wild-type cells under normal growth conditions, by allowing productive extrusion from multiple neighboring *parS* sites.

## Discussion

Thus, a model where SMC complexes can traverse one another on the chromosome after momentary pausing is consistent with results from many strains and conditions tested here (Fig. 7). Our study demonstrates that, by harnessing the SMC-ParB-*parS* system, we can create complex chromosome folding patterns not seen before in natural systems, which help understand what is happening in the wild-type cells. Strikingly, these structures could be predicted by a quantitative model of SMC dynamics, which was central to identifying the bypassing mechanism as a key feature of *B. subtilis* SMC loop extrusion. We inferred that SMC complexes can traverse past each other within  $\sim 20$  s of an encounter *in vivo*. This timescale is consistent with the *in vitro* times of  $\sim 8$  s measured by single-molecule experiments for yeast condensins to traverse past one another on naked DNA<sup>23</sup>. These times are also consistent with the  $\sim 10$  s in *B. subtilis* to traverse sites of active transcription, as shown previously<sup>29</sup>. Together, these results suggest that the phenomenon of

SMCs traversing past one another, and other steric obstacles, may be general to many species and processes.

In specific situations, we found it is possible to overwhelm the bypassing mechanism and create SMC traffic jams. The jamming, caused by elevated numbers of chromosome-bound SMC complexes, is similar to the phenomenon where high RNA polymerase traffic (that opposes the direction of SMC translocation, for example, at rRNA genes) leads to the accumulation (and pausing) of loop extruders at transcription end sites<sup>9,29,34</sup>. At first glance, SMC complexes bypassing each other to form structures such as Z-loops appear to tangle the DNA. However, bypassing generally helps avoid traffic jams formed with SMCs loaded at adjacent sites. This is important in bacteria, because *parS* sites often occur in multiple copies close to the *ori*<sup>19</sup>. A recent study<sup>35</sup> proposed that SMCs do not collide frequently in *B. subtilis*. However, our quantitative analysis indicates that SMCs collide very often in wild-type cells; with an estimated number of 15–30 SMC complexes per chromosome, a collision event between SMCs is expected on average at least once a minute (Fig. 6b). Thus, if bypassing were not a feature of SMC complexes in wild-type *B. subtilis* cells, then pervasive tethers between the *ori* and other genome positions would frequently occur, potentially affecting *ori* segregation (Extended Data Fig. 10b). To minimize such long-range tethers, *B. subtilis* cells would have to organize chromosomes with no more than four SMC complexes

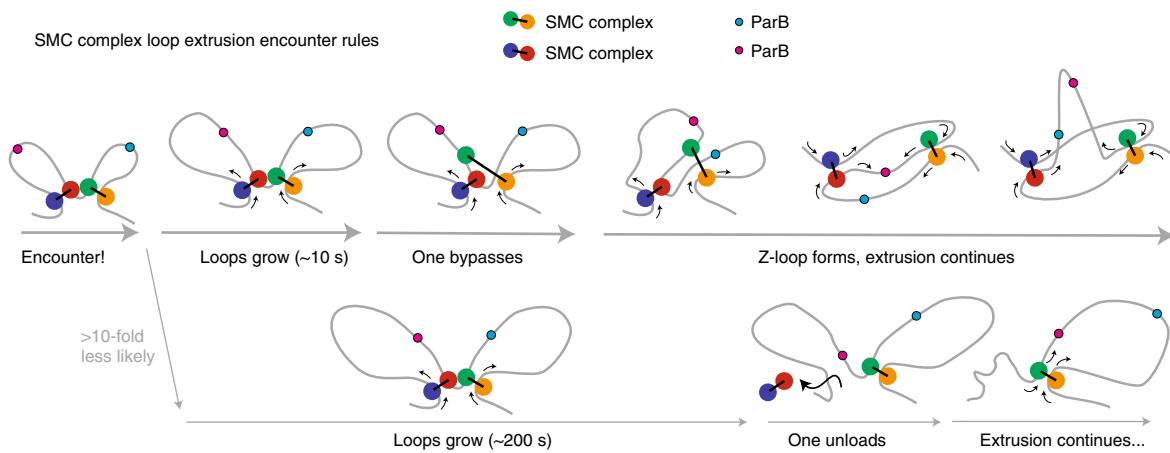


**Fig. 7 | Schematic model illustrating how SMC encounters are resolved.** In an encounter, SMC complexes first mutually block one another and then may resolve the conflict either by bypassing (top row) or unloading from the DNA (bottom row). The bypassing mode of conflict resolution occurs at least 10 times more frequently than unloading (indicated by the thickness of the arrows).

per chromosome (that is, <20% of experimentally measured values<sup>32</sup>). In such a case, however, the chromosome arm juxtaposition is poor, as seen by simulations (Extended Data Fig. 10b), and much weaker than seen experimentally<sup>26</sup>. Moreover, even with as few as five SMCs per chromosome, at least one collision event is expected every 10 min for every chromosome (Fig. 6b). Thus, in addition to mechanisms that may help fine-tune the numbers of SMCs per chromosome<sup>35</sup>, bypassing appears to be an essential property that allows multiple *parS* sites to function together efficiently, not only in engineered strains, but also in wild-type cells under exponential growth conditions.

In eukaryotes, bypassing can help promote chromosome compaction and sister-chromatid segregation<sup>30,36</sup>. However, we hypothesize that bypassing could have a function beyond compaction and segregation. For example, bypassing of obstacles and other SMC complexes could potentially facilitate spreading of *cis*-related chromatin marks (for example, around a DNA double-strand break<sup>37–39</sup>) or help trafficking of various factors along the chromosome<sup>40–42</sup>. Speculatively, if the ability to bypass obstacles is rampant, cells may have developed specific mechanisms to control this process and stop extrusion (for example, CTCF proteins for cohesins<sup>43</sup>).

Recent biochemical, cryo-EM and atomic force microscopy (AFM) studies indicate that the SMC complexes are flexible and dynamic<sup>44–46</sup>, but the underlying molecular mechanism of loop extrusion remains elusive. A future challenge of the field is to investigate the molecular mechanism of bypassing using biochemical and structural approaches. In addition, single-molecule approaches will be powerful to determine the ability and efficiency of various SMC complexes to bypass one another, as shown previously<sup>23</sup>. However, the targeted SMC complex loading approach (as we have shown here) can produce distinct signatures visible by Hi-C that can help distinguish bypassing from other mechanisms. Employing this idea in a eukaryotic system like *Caenorhabditis elegans*<sup>47</sup> could be very powerful to investigate if bypassing occurs *in vivo* in eukaryotes.

In summary, we have shown that *B. subtilis* SMC complexes can resolve encounters by simply translocating past one another, allowing them to spatially organize a functional and busy genome.

## Online content

Any methods, additional references, Nature Research reporting summaries, source data, extended data, supplementary information, acknowledgements, peer review information; details of author contributions and competing interests; and statements of data and code availability are available at <https://doi.org/10.1038/s41594-021-00626-1>.

Received: 14 December 2020; Accepted: 17 June 2021;  
Published online: 26 July 2021

## References

- Hirano, T. Condensins: universal organizers of chromosomes with diverse functions. *Genes Dev.* **26**, 1659–1678 (2012).
- Yatskevich, S., Rhodes, J. & Nasmyth, K. Organization of chromosomal DNA by SMC complexes. *Annu. Rev. Genet.* **53**, 445–482 (2019).
- Davidson, I. F. et al. DNA loop extrusion by human cohesin. *Science* **366**, 1338–1345 (2019).
- Ganji, M. et al. Real-time imaging of DNA loop extrusion by condensin. *Science* **360**, 102–105 (2018).
- Golfier, S., Quail, T., Kimura, H. & Brugués, J. Cohesin and condensin extrude DNA loops in cell cycle-dependent manner. *Elife* **9**, e53885 (2020).
- Kim, Y., Shi, Z., Zhang, H., Finkelstein, I. J. & Yu, H. Human cohesin compacts DNA by loop extrusion. *Science* **366**, 1345–1349 (2019).
- Kong, M. et al. Human condensin I and II drive extensive ATP-dependent compaction of nucleosome-bound DNA. *Mol. Cell* **79**, 99–114 (2020).
- Terakawa, T. et al. The condensin complex is a mechanochemical motor that translocates along DNA. *Science* **358**, 672–676 (2017).
- Tran, N. T., Laub, M. T. & Le, T. B. K. SMC progressively aligns chromosomal arms in *Caulobacter crescentus* but is antagonized by convergent transcription. *Cell Rep.* **20**, 2057–2071 (2017).
- Wang, X., Brandão, H. B., Le, T. B., Laub, M. T. & Rudner, D. Z. *Bacillus subtilis* SMC complexes juxtapose chromosome arms as they travel from origin to terminus. *Science* **355**, 524–527 (2017).
- Wang, X. et al. In vivo evidence for ATPase-dependent DNA translocation by the *Bacillus subtilis* SMC condensin complex. *Mol. Cell* **71**, 841–847 (2018).
- Banigan, E. J. & Mirny, L. A. Loop extrusion: theory meets single-molecule experiments. *Curr. Opin. Cell Biol.* **64**, 124–138 (2020).
- Fudenberg, G., Abdennur, N., Imakaev, M., Goloborodko, A. & Mirny, L. A. Emerging evidence of chromosome folding by loop extrusion. *Cold Spring Harb. Symp. Quant. Biol.* **82**, 45–55 (2017).
- Böhm, K. et al. Chromosome organization by a conserved condensin-ParB system in the actinobacterium *Corynebacterium glutamicum*. *Nat. Commun.* **11**, 1485 (2020).
- Gruber, S. & Errington, J. Recruitment of condensin to replication origin regions by ParB/SpoOJ promotes chromosome segregation in *B. subtilis*. *Cell* **137**, 685–696 (2009).
- Lioy, V. S., Junier, I., Lagage, V., Vallet, I. & Boccard, F. Distinct activities of bacterial condensins for chromosome management in *Pseudomonas aeruginosa*. *Cell Rep.* **33**, 108344 (2020).
- Minnen, A. et al. Control of Smc coiled coil architecture by the ATPase heads facilitates targeting to chromosomal ParB/*parS* and release onto flanking DNA. *Cell Rep.* **14**, 2003–2016 (2016).
- Sullivan, N. L., Marquis, K. A. & Rudner, D. Z. Recruitment of SMC by ParB-*parS* organizes the origin region and promotes efficient chromosome segregation. *Cell* **137**, 697–707 (2009).
- Livny, J., Yamaichi, Y. & Waldor, M. K. Distribution of centromere-like *parS* sites in bacteria: insights from comparative genomics. *J. Bacteriol.* **189**, 8693–8703 (2007).
- Lioy, V. S. et al. Multiscale structuring of the *E. coli* chromosome by nucleoid-associated and condensin proteins. *Cell* **172**, 771–783 (2018).

21. Mäkelä, J. & Sherratt, D. J. Organization of the *Escherichia coli* chromosome by a MukBEF axial core. *Mol. Cell* **78**, P250–P260 (2020).
22. Alipour, E. & Marko, J. F. Self-organization of domain structures by DNA-loop-extruding enzymes. *Nucleic Acids Res.* **40**, 11202–11212 (2012).
23. Kim, E., Kerssemakers, J., Shaltiel, I. A., Haering, C. H. & Dekker, C. DNA-loop extruding condensin complexes can traverse one another. *Nature* **579**, 438–442 (2020).
24. Breier, A. M. & Grossman, A. D. Whole-genome analysis of the chromosome partitioning and sporulation protein Spo0J (ParB) reveals spreading and origin-distal sites on the *Bacillus subtilis* chromosome. *Mol. Microbiol.* **64**, 703–718 (2007).
25. Marbouty, M. et al. Condensin- and replication-mediated bacterial chromosome folding and origin condensation revealed by Hi-C and super-resolution imaging. *Mol. Cell* **59**, 588–602 (2015).
26. Wang, X. et al. Condensin promotes the juxtaposition of DNA flanking its loading site in *Bacillus subtilis*. *Genes Dev.* **29**, 1661–1675 (2015).
27. Wagner, J. K., Marquis, K. A. & Rudner, D. Z. SirA enforces diploidy by inhibiting the replication initiator DnaA during spore formation in *Bacillus subtilis*. *Mol. Microbiol* **73**, 963–974 (2009).
28. Le, T. B., Imakaev, M. V., Mirny, L. A. & Laub, M. T. High-resolution mapping of the spatial organization of a bacterial chromosome. *Science* **342**, 731–734 (2013).
29. Brandão, H. B. et al. RNA polymerases as moving barriers to condensin loop extrusion. *Proc. Natl Acad. Sci. USA* **116**, 20489–20499 (2019).
30. Banigan, E. J., van den Berg, A. A., Brandão, H. B., Marko, J. F. & Mirny, L. A. Chromosome organization by one-sided and two-sided loop extrusion. *Elife* **9**, e53558 (2020).
31. Miernans, C. A. & Broedersz, C. P. Bacterial chromosome organization by collective dynamics of SMC condensins. *J. R. Soc. Interface* **15**, 20180495 (2018).
32. Wilhelm, L. et al. SMC condensin entraps chromosomal DNA by an ATP hydrolysis dependent loading mechanism in *Bacillus subtilis*. *Elife* **4**, e06659 (2015).
33. Sueoka, N. & Yoshikawa, H. The chromosome of *Bacillus subtilis*. I. Theory of marker frequency analysis. *Genetics* **52**, 747–757 (1965).
34. Vazquez Nunez, R., Ruiz Avila, L. B. & Gruber, S. Transient DNA occupancy of the SMC interarm space in prokaryotic condensin. *Mol. Cell* **75**, 209–223 (2019).
35. Anchimiuk, A., Lioy, V. S., Minnen, A., Boccard, F. & Gruber, S. Fine-tuning of the Smc flux facilitates chromosome organization in *B. subtilis*. Preprint at *bioRxiv* <https://doi.org/10.1101/2020.12.04.411900> (2020).
36. He, Y. et al. Statistical mechanics of chromosomes: in vivo and in silico approaches reveal high-level organization and structure arise exclusively through mechanical feedback between loop extruders and chromatin substrate properties. *Nucleic Acids Res.* **48**, 11284–11303 (2020).
37. Arnould, C. et al. Loop extrusion as a mechanism for formation of DNA damage repair foci. *Nature* **590**, 660–665 (2021).
38. Li, K., Bronk, G., Kondev, J. & Haber, J. E. Yeast ATM and ATR kinases use different mechanisms to spread histone H2A phosphorylation around a DNA double-strand break. *Proc. Natl Acad. Sci. USA* **117**, 21354–21363 (2020).
39. Liu, Y. et al. Very fast CRISPR on demand. *Science* **368**, 1265–1269 (2020).
40. Anderson, E. C. et al. X Chromosome domain architecture regulates *Caenorhabditis elegans* lifespan but not dosage compensation. *Dev. Cell* **51**, 192–207 (2019).
41. Collins, P. L. et al. DNA double-strand breaks induce H2Ax phosphorylation domains in a contact-dependent manner. *Nat. Commun.* **11**, 3158 (2020).
42. Wang, C. Y., Colognori, D., Sunwoo, H., Wang, D. & Lee, J. T. PRC1 collaborates with SMCHD1 to fold the X-chromosome and spread Xist RNA between chromosome compartments. *Nat. Commun.* **10**, 2950 (2019).
43. Heger, P., Marin, B., Bartkuhn, M., Schierenberg, E. & Wiehe, T. The chromatin insulator CTCF and the emergence of metazoan diversity. *Proc. Natl Acad. Sci. USA* **109**, 17507–17512 (2012).
44. Lee, B. G. et al. Cryo-EM structures of holo condensin reveal a subunit flip-flop mechanism. *Nat. Struct. Mol. Biol.* **27**, 743–751 (2020).
45. Higashi, T. L. et al. A structure-based mechanism for DNA entry into the cohesin ring. *Mol. Cell* **79**, 917–933 (2020).
46. Ryu, J. K. et al. The condensin holocomplex cycles dynamically between open and collapsed states. *Nat. Struct. Mol. Biol.* **27**, 1134–1141 (2020).
47. Jimenez, D. S. et al. Condensin DC spreads linearly and bidirectionally from recruitment sites to create loop-anchored TADs in *C. elegans*. Preprint at *bioRxiv* <https://doi.org/10.1101/2021.03.23.436694> (2021).

**Publisher's note** Springer Nature remains neutral with regard to jurisdictional claims in published maps and institutional affiliations.

© The Author(s), under exclusive licence to Springer Nature America, Inc. 2021

## Methods

**General methods.** The *B. subtilis* strains were derived from the prototrophic strain PY79<sup>18</sup>. Cells were grown in defined rich medium (CH)<sup>49</sup> at 37 °C with aeration. Cells were arrested at G1 phase by expressing SirA<sup>27</sup> for the indicated durations using IPTG at a final concentration of 1 mM or xylose at 0.5%. A list of next-generation sequencing samples is provided in Supplementary Table 1, arranged by the figure in which they appear. Lists of strains, plasmids and oligonucleotides are provided in Supplementary Tables 2–4. Unprocessed microscopy images and uncropped western blots are available in Mendeley Data (<https://doi.org/10.17632/vgw8sjxsvy.1>).

**Hi-C.** The detailed Hi-C procedure has been described previously<sup>26</sup>. Briefly, 5 × 10<sup>7</sup> cells were crosslinked with 3% formaldehyde at room temperature for 30 min then quenched with 125 mM glycine. Cells were lysed using Ready-Lyse Lysozyme (Epicentre, R1802M) followed by 0.5% SDS treatment. Solubilized chromatin was digested with HindIII for 2 h at 37 °C. The cleaved ends were filled in with Klenow and biotin-14-dATP, dGTP, dCTP and dTTP. The products were ligated in dilute reactions with T4 DNA ligase overnight at 16 °C. Crosslinks were reversed at 65 °C overnight in the presence of proteinase K. The DNA was then extracted twice with phenol/chloroform/isoamylalcohol (25:24:1, PCI), precipitated with ethanol, and resuspended in 20 µl of Qiagen EB buffer. Biotin from non-ligated ends was removed using T4 polymerase (4 h at 20 °C) followed by extraction with PCI. The DNA was then sheared by sonication for 12 min with 20% amplitude using a Qsonica Q800R2 water bath sonicator. The sheared DNA was used for library preparation with the NEBNext UltraII kit (E7645) according to the manufacturer's instructions for end repair, adapter ligation and size selection. Biotinylated DNA fragments were purified using 5 µl streptavidin beads (Invitrogen, 65001), then the DNA-bound beads were used for polymerase chain reaction (PCR) in a 50-µl reaction for 14 cycles. PCR products were purified using Ampure beads and sequenced at the Indiana University Center for Genomics and Bioinformatics using NextSeq550. Paired-end sequencing reads were mapped to the genome of *B. subtilis* PY79 (NCBI reference sequence NC\_022898.1) using the same pipeline described in ref. <sup>26</sup>. The *B. subtilis* PY79 genome was first divided into 404 10-kb bins. Subsequent analysis and visualization was done using R and Python scripts. The genetic loci marked by degree (°) were calculated using the PY79 genome, which results in a slight shift from data published using *B. subtilis* 168 genomic coordinates.

**Chromatin immunoprecipitation sequencing.** ChIP sequencing was performed as described previously<sup>26</sup>. Briefly, cells were crosslinked using 3% formaldehyde for 30 min at room temperature and then quenched, washed and lysed. Chromosomal DNA was sheared to an average size of 250 bp by sonication using a Qsonica Q800R2 water bath sonicator. The lysate was then incubated overnight at 4 °C with anti-SMC<sup>50</sup> antibodies, and was subsequently incubated with Protein A-Sepharose (GE HealthCare) for 1 h at 4 °C. After washes and elution, the immunoprecipitate was incubated at 65 °C overnight to reverse the crosslinks. The DNA was further treated with RNase A, Proteinase K, extracted with PCI, resuspended in 50 µl of EB buffer and used for library preparation with the NEBNext UltraII kit (E7645) and sequenced using the Illumina MiSeq or NextSeq550 platforms. The sequencing reads were aligned to the *B. subtilis* PY79 genome (NCBI NC\_022898.1) using CLC Genomics Workbench (CLC Bio, Qiagen), and subsequently normalized, plotted and analyzed using R and Python scripts.

**Whole-genome sequencing for DNA replication profiling.** Cells were grown and collected at the indicated time points. Genomic DNA was extracted using the QIAgen DNeasy Blood and Tissue kit (Qiagen cat. no. 69504). DNA was sonicated using a Qsonica Q800R2 sonicator for 12 min at 20% amplitude to achieve an average fragment size of 250 bp. The DNA library was prepared using an NEBNext UltraII kit (NEB E7645), and sequenced using Illumina NextSeq550. Sequencing reads were mapped to the *B. subtilis* PY79 genome (NCBI reference sequence NC\_022898.1) using CLC Genomics Workbench (Qiagen). The mapped reads were normalized to the total number of reads for that sample and plotted in R or Python using matplotlib 3.2.0.

**Microscopy.** Fluorescence microscopy was performed on a Nikon Ti2E microscope equipped with a Plan Apo ×100/1.4-NA phase contrast oil objective and an sCMOS camera. Images were acquired using Nikon Elements software. Cells were immobilized using 2% agarose pads containing growth medium. Membranes were stained with FM4-64 (Molecular Probes) at 3 µg ml<sup>-1</sup>. DNA was stained with DAPI at 2 µg ml<sup>-1</sup>. Images were cropped, linearly adjusted and analyzed using MetaMorph software (Molecular Devices). Final figures were prepared in Adobe Illustrator.

**Immunoblot analysis.** Cells were collected at appropriate time points and resuspended in lysis buffer (20 mM Tris pH 7.0, 1 mM EDTA, 10 mM MgCl<sub>2</sub>, 1 mg ml<sup>-1</sup> lysozyme, 10 µg ml<sup>-1</sup> DNase I, 100 µg ml<sup>-1</sup> RNase A, 1 mM PMSF and 1% proteinase inhibitor cocktail (Sigma P-8340)) to a final optical density at 600 nm of 10 for equivalent loading. The cell resuspensions were incubated at 37 °C for 10 min for lysozyme treatment, and followed by the addition of an

equal volume of 2× Laemmli sample buffer (Bio-Rad 1610737) containing 10% β-mercaptoethanol. Samples were heated for 5 min at 80 °C before loading. Proteins were separated by precast 4–20% polyacrylamide gradient gels (Bio-Rad 4561096), electroblotted onto mini PVDF membranes using a Bio-Rad Transblot Turbo system and reagents (Bio-Rad 1704156). The membranes were blocked in 5% nonfat milk in phosphate-buffered saline (PBS) with 0.5% Tween 20, and then probed with anti-ParB (1:5,000)<sup>51</sup>, anti-SMC (1:5,000)<sup>50</sup>, anti-SigA (1:10,000)<sup>52</sup>, anti-ScpA (1:10,000)<sup>10</sup> or anti-ScpB (1:10,000)<sup>10</sup> diluted into 3% BSA in 1× PBS with 0.05% Tween 20. Primary antibodies were detected using Immun-Star horseradish peroxidase-conjugated goat anti-rabbit antibodies (Bio-Rad 1705046) and Western Lightning Plus ECL chemiluminescence reagents (Perkin Elmer NEL1034001) as described by the manufacturer. The signal was captured using a ProteinSimple FluorChem R system. The intensity of the bands was quantified using ProteinSimple AlphaView software.

**Plasmid construction.** pWX512 [*amyE::Phyperspank-(optRBS)-smc (spec)*] was generated by inserting *smc* with an optimal ribosome binding site (*optRBS*) (amplified using oWX516 and oWX517 from *B. subtilis* PY79 genome and digested with NheI and SphI) into pdr111 [*amyE::Phyperspan (spec)*] (D. Z. Rudner, unpublished) between NheI and SphI. The construct was sequenced using oWX486, oWX524, oWX848, oWX1194, oWX1195 and oWX1196.

pWX777 [*yhdG::Pxyl-(optRBS)-sirA (phleo)*] was generated by inserting *sirA* with an optimal ribosome binding site (*optRBS*) (amplified using oWX1892 and oWX1893 from *B. subtilis* PY79 genome and digested with HindIII and NheI) into pMS25 [*yhdG::Pxyl (phleo)*] (D. Z. Rudner, unpublished) between HindIII and NheI. The construct was sequenced using oML87 and oWX1894.

pWX778 [*yhdG::Phyperspank-(optRBS)-scpAB (phleo)*] was generated by inserting *scpAB* with an optimal ribosome binding site (*optRBS*) (amplified using oWX1897 and oWX1898 from *B. subtilis* PY79 genome and digested with HindIII and NheI) into pMS28 [*yhdG::Phyperspank (phleo)*] (D. Z. Rudner, unpublished) between HindIII and NheI. The construct was sequenced using oWX428, oWX486 and oWX487.

pWX788 [*yhdG::Phyperspank-(optRBS)-sirA (erm)*] was generated by inserting *sirA* with an optimal ribosome binding site (*optRBS*) (amplified using oWX1892 and oWX1893 from *B. subtilis* PY79 genome and digested with HindIII and NheI) into pMS24 [*yhdG::Phyperspank (erm)*] (D. Z. Rudner, unpublished) between HindIII and NheI. The construct was sequenced using oWX486 and oWX524.

**Strain construction.** For −91°*parS loxP-kan-loxP* (BWX3379), the +4° *parS* sequence (TGTTACACGTGAAACA) was inserted at −91° (in the intergenic region between *ktrB* and *yubF*). An isothermal assembly product was directly transformed to *parS*A9 (BWX3212)<sup>26</sup>, which has all nine *parS* sites deleted from the *B. subtilis* genome. The isothermal assembly reaction contained three PCR products: (1) a region containing *ktrB* (amplified from PY79 genomic DNA using oWX1279 and oWX1280); (2) the *loxP-kan-loxP* cassette flanked by the +4° *parS* sequence (amplified from pWX470 using universal primers oWX1241 and oWX438); (3) a region containing *yubF* (amplified from PY79 genomic DNA using primers oWX1281 and oWX1282). The transformants were amplified and sequenced using oWX1283 and oWX1284.

Multiple *parS* sites were combined by standard transformation protocols. The *loxP-kan-loxP* cassette was removed using a *cre*-expressing plasmid pDR244<sup>53</sup>, resulting in an unmarked *parS* site indicated as ‘no a.b.’

**Calculation of SMC number and error estimation.** The number of SMC complexes was calculated from marker frequency analysis, fluorescence microscopy and immunoblotting experiments. The calculation and error estimation are provided in Supplementary Data 1.

**Comparison of simulated and experimental Hi-C contact maps.** To compare the simulated maps to the experimental maps, we quantified both the interaction frequencies that give the intensities of pixels and the angle/tilt of the lines. For interaction frequencies/intensities, we use contact probability decay  $P_s(s)$  as a function of genomic distance,  $s$ , as seen in Supplementary Figs. 5–7.  $P_s(s)$  has been a gold-standard method for comparison between Hi-C and simulations<sup>28,54,55</sup>. We also used the same color scales for the simulations and experiments to visually compare the intensities of the various lines. To quantify the angle/tilt of the lines, we drew lines on the plots (for example, Extended Data Fig. 2) and matched the angles between simulations and experiments—these were used as input into our mathematical models (Supplementary Notes 1–5). For the contact probability decay curves, the best-fit values were identified as

$$\text{Goodness of fit for } P(s) = \frac{1}{M} \sum_s^M \left| \log(P(s)_{\text{experiment}}) - \log(P(s)_{\text{simulation}}) \right|$$

where  $M$  is the number of points used to plot the  $P(s)$  curves, and  $s$  is the specified genomic distance. For the intensity of line 1 compared to background levels, we quantified the line 1 and background intensities by computing the mean contact frequency within a ‘box’ centered on line 1 or away from line 1

(Supplementary Fig. 6c). The contact frequency within the boxes was computed (using Python notation) as

```
Background box value = numpy.mean(A[250 : 300, 300 : 350])
Line1 box value      = numpy.mean(A[286 : 337, 337 : 387])
```

where  $A$  is the  $404 \times 404$  *ter*-centered Hi-C contact frequency matrix. The ratio of the line 1 box value to the background box values was computed for each simulation, and compared to the experimental value of 2.66. To obtain the *parS* loading strength, we minimized

$$\text{Goodness of fit for Line 1} = |(\text{Line 1 box value}) / (\text{Background box value}) - 2.66|$$

**Simulations and model generation.** All details on simulations and polymer modeling are provided in Supplementary Notes 1–5.

**Finding the optimal model parameters that match experimental data.** To obtain the best parameters for our model to match the experimental data, we used both ChIP-seq and Hi-C results. We employed a combination of quantitative measurements and semi-qualitative measurements. For quantitative measurements, we (1) compared simulated to experimental Hi-C contact maps by calculating the absolute difference between the simulated and experimental contact probability decay curves, (2) calculated the contact frequency of line 1 relative to its background contact frequency and (3) measured the angles of the Hi-C lines 1 and 2 from experiments (Fig. 2a). These quantitative measures helped us choose the best-fit values (Supplementary Figs. 5 and 6) and were used as quantitative constraints in a mathematical model that related several model parameters to one another. For semi-qualitative measurements, we carried out a visual inspection to match the numerical values and the overall shapes of ChIP-seq profiles between simulations and experiments (Supplementary Fig. 4).

In total, we needed to obtain six core parameters: (1) *parS*-specific loading rates (that is, *parS* strength), (2) the number of LEFs per chromosome, (3) spontaneous dissociation rate, (4) terminus-specific dissociation rate, (5) facilitated dissociation rate (that is, the unloading rate) and (6) bypassing rate. We performed simulations to systematically vary several parameters (that is, we performed parameter sweeps). We did not sweep all six parameters independently as we found that their values could be mathematically constrained relative to one another. We narrowed down the space of parameter values to four independent values (1–4 above). As we swept those values, we compared various characteristics of our resulting model to Hi-C and ChIP-seq data for various strains. The process is detailed in the following.

1. We first sought to determine the spontaneous dissociation rate. We performed simulations of LEF distributions (Supplementary Fig. 4) and varied three parameters: the number of LEFs per chromosome, the spontaneous dissociation rate of LEFs and the bypassing rate. At this step we assumed specific values for other parameters (including *parS*-specific loading rate and facilitated dissociation rate) that are varied later. We compared the simulated LEF profiles to SMC ChIP-seq results for a strain containing a single *parS* site near the *ori*. We found that spontaneous dissociation rates below a certain value (<1 per 1,260 s) were necessary to reproduce the steady decay of SMC occupancy from the *ori* to *ter* that is observed experimentally (Supplementary Fig. 4). Within the range of dissociation rate values of ~1 per 2,560 s to 1 per 1,260 s, the simulated LEF distribution profiles were in good visual agreement with the ChIP-seq curves for a broad range of bypassing rates and the numbers of LEFs. Thus, after these simulations, we fixed the spontaneous dissociation rate to 1 per 2,560 s (that is,  $0.0004\text{s}^{-1}$  or 1 per 43 min) as a default value. This reciprocal of this rate (43 min) is also approximately the time for an SMC complex to travel from the *ori* to the *ter*. As a comparison, in our growth condition, it takes ~40 min for a LEF to travel from the *ori* to the *ter*, as measured previously<sup>10</sup>.
2. The terminus-specific dissociation rate was chosen qualitatively to give a ‘smooth decay’ of LEF occupancy near the *ter*, and a smooth decay of lines 1 and 2 at the terminus region as seen in Hi-C maps. This parameter did not affect the results above, but shaped the qualitative agreement between the simulated and experimental Hi-C maps and the ChIP-seq curves. Specifically, the 1-kb monomers at the terminus region (1950–2050) are given a dissociation rate of approximately fivefold of the spontaneous dissociation rate, at  $0.0025\text{s}^{-1}$ . Future extensions to better simulate the *ter* region may incorporate the recently discovered site-specific unloading of SMCs at XerD-binding sites (XDS sites)<sup>36</sup>.
3. We next developed a theoretical framework to understand the relationship between the bypassing rate, the facilitated dissociation rate, the *parS*-specific loading rate and the numbers of LEFs per chromosome. The *parS*-specific loading rate and the number of LEFs per chromosome dramatically affect the frequency of LEF collisions. We found that the bypassing rate and the frequency of LEF collisions are constrained relative to each other by a constant (Supplementary Note 5, ‘Relationship between the bypassing rate, number of LEFs and the tilt of Line 1’ and ‘Estimating the bypassing rate from the number of SMC complexes’ for calculations). On the Hi-C map, these parameters

are responsible for modulating the relative tilts observed for lines 1 and 2. Thus, by measuring the angles subtended by lines 1 and 2, we constrained the bypassing rate relative to the number of LEFs and the *parS*-specific loading rate. Moreover, we found that the facilitated dissociation rate could also be constrained relative to the bypassing rate and the frequency of collisions of LEFs; these parameters are also related to one another by a constant, and are estimated by the relative intensities of lines 3 and 4 (Supplementary Note 5, ‘The frequency of nested-doublet interactions is controlled by the ratio of bypassing rates to unloading rates’). We provide examples in Extended Data Figs. 4 and 5 to show the trade-off between the facilitated dissociation rate and bypassing rate in modulating the line 3 and 4 intensities. In summary, from our analytical considerations, we found that, instead of having to independently sweep and fit four parameters (bypassing rate, the facilitated dissociation rate, the *parS*-specific loading rate and the numbers of LEFs per chromosome), we only needed to determine two of them to get all four.

4. We next found the number of LEFs per chromosome and the *parS*-specific loading rate using Hi-C maps. We fit the contact probability decay curve from experiments to those generated by our model (Supplementary Figs. 5 and 6), and also compared the relative intensity of line 1, measured as the contact frequency of a box centered on line 1 compared to a background level of contacts (Supplementary Fig. 6). From these comparisons (detailed below), we were able to constrain both the number of LEFs and the *parS*-specific loading rate (Supplementary Figs. 5–7): briefly, we simultaneously varied the number of LEFs per chromosome and the *parS*-specific loading rate, and used the analytical constraints for the bypassing rate and facilitated dissociation rate. We matched the shapes and values of the Hi-C contact probability decay curves ( $P_c(s)$ ) by comparing simulations to experiments (Supplementary Figs. 5–7). For a strain with no *parS* sites, we identified that ~30–40 LEFs were needed to best match the shapes and numerical values of the  $P_c(s)$  curves (Supplementary Fig. 5) as judged by minimizing the goodness-of-fit metric (see the calculations in the section ‘Comparison of simulated and experimental Hi-C contact maps’). We also simulated strains with single *parS* sites: we found that it was the number of ‘off-target’ (non-*parS* loaded) SMC complexes that largely governed the overall shape and numerical values of the  $P_c(s)$ . By contrast, the number of ‘on-target’ (that is, *parS*-loaded) LEFs largely influenced the intensity of line 1 and not the  $P_c(s)$  curve (Supplementary Fig. 6a). The overall best-matching  $P_c(s)$  curves (as judged by the goodness-of-fit metric) had ~20 ‘off-target’ LEFs (Supplementary Fig. 6b). Moreover, the visually and quantitatively best-matching line 1 intensities corresponded to ~20 ‘on-target’ LEFs (Supplementary Fig. 6c). Together, these results suggest ~40 LEFs per chromosome, which is similar to the value identified in Supplementary Fig. 5. In addition, these data indicate that the relative probability of a LEF loading at a *parS* lattice site is 4,000 times stronger than at non-*parS* sites (that is, a *parS*-specific loading strength of ~4,000). As a self-consistency check for these two parameters (that is, number of LEFs of ~40 and strength of *parS* sites of ~4,000), we compared the  $P_c(s)$  curve and line intensities for a strain with two *parS* sites. We found a good visual agreement between experiment and simulation for the  $P_c(s)$  curves, as well as the relative intensities of lines 1, 2 and 3 (Supplementary Fig. 7).
5. With the finding that there are ~30–40 LEFs per chromosome and a *parS*-specific loading rate of 4,000, using our quantitative constraints discussed in (3), we automatically obtained the bypassing rate (in the range of  $0.03\text{--}0.05\text{s}^{-1}$ , that is, pausing for 20–30 s before bypassing) and the facilitated unloading rate (in the range  $\sim0.001\text{--}0.005\text{s}^{-1}$ ).

**Reporting Summary.** Further information on research design is available in the Nature Research Reporting Summary linked to this Article.

## Data availability

Plasmids and strains generated in this study are available from X.W. with a completed materials transfer agreement. Hi-C and ChIP-seq data that support the findings of this study have been deposited in the Gene Expression Omnibus with accession no. GSE155279. All next-generation sequencing data used in this study are listed and itemized in Supplementary Table 1 with the corresponding accession numbers. Unprocessed microscopy images, uncropped blot images and their associated molecular weight/size markers can be accessed in Mendeley Data at <https://doi.org/10.17632/vgw8sjxsvy.1>.

## Code availability

Simulation codes used to generate Hi-C-like contact maps and SMC ChIP-seq-like occupancy profiles in this paper are available on Zenodo at <https://doi.org/10.5281/zenodo.4918358> and also in the GitHub repository <https://github.com/hbbrandao/bacterialSMCTrajectories>.

## References

48. Youngman, P. J., Perkins, J. B. & Losick, R. Genetic transposition and insertional mutagenesis in *Bacillus subtilis* with *Streptococcus faecalis* transposon Tn917. *Proc. Natl Acad. Sci. USA* **80**, 2305–2309 (1983).

49. Harwood, C. R. & Cutting, S. M. (eds) *Molecular Biological Methods for Bacillus* (Wiley, 1990).
50. Lindow, J. C., Kuwano, M., Moriya, S. & Grossman, A. D. Subcellular localization of the *Bacillus subtilis* structural maintenance of chromosomes (SMC) protein. *Mol. Microbiol.* **46**, 997–1009 (2002).
51. Lin, D. C., Levin, P. A. & Grossman, A. D. Bipolar localization of a chromosome partition protein in *Bacillus subtilis*. *Proc. Natl Acad. Sci. USA* **94**, 4721–4726 (1997).
52. Fujita, M. Temporal and selective association of multiple sigma factors with RNA polymerase during sporulation in *Bacillus subtilis*. *Genes Cells* **5**, 79–88 (2000).
53. Meeske, A. J. et al. MurJ and a novel lipid II flippase are required for cell wall biogenesis in *Bacillus subtilis*. *Proc. Natl Acad. Sci. USA* **112**, 6437–6442 (2015).
54. Di Stefano, M., Nutzmann, H. W., Marti-Renom, M. A. & Jost, D. Polymer modelling unveils the roles of heterochromatin and nucleolar organizing regions in shaping 3D genome organization in *Arabidopsis thaliana*. *Nucleic Acids Res.* **49**, 1840–1858 (2021).
55. Fudenberg, G. et al. Formation of chromosomal domains by loop extrusion. *Cell Rep.* **15**, 2038–2049 (2016).
56. Karaboja, X. et al. XerD unloads bacterial SMC complexes at the replication terminus. *Mol. Cell* **81**, 756–766 (2021).

### Acknowledgements

We thank M. Imakaev and A. Goloborko for the development of the polychrom simulation package, as well as E. Banigan, A. van den Berg, K. Polovnikov, Q. Liao and E. Schantz for discussions. We are grateful to S. Gruber, C. Broedersz, J. Dekker and J. Harju for critically evaluating our manuscript and exchanging ideas. We thank M. Suiter for strain building, Indiana University Center for Genomics and Bioinformatics for assistance with high throughput sequencing, A. Grossman for anti-SMC and anti-ParB antibodies,

and D. Rudner for plasmids and anti-ScpA, anti-ScpB and anti-SigA antibodies. Support for this work comes from National Institute of Health grants R01GM141242 to X.W. and U01CA200147 and R01GM114190 to L.A.M. H.B.B. was partially supported by a Natural Sciences and Engineering Research Council of Canada Post-Graduate Fellowship (Doctoral). We also acknowledge support from the National Institutes of Health Common Fund 4D Nucleome Program (DK107980) to L.A.M. and H.B.B.

### Author contributions

H.B.B. and X.W. conceived the project. H.B.B. developed the theory and models and analyzed data with L.A.M., with input from X.W. Z.R. and X.W. performed Hi-C experiments and analyses. X.K. and X.W. constructed strains and performed and analyzed ChIP-seq, whole-genome sequencing, fluorescence microscopy and immunoblot experiments. H.B.B., L.A.M. and X.W. interpreted results and wrote the manuscript, with input from all authors.

### Competing interests

The authors declare no competing interests.

### Additional information

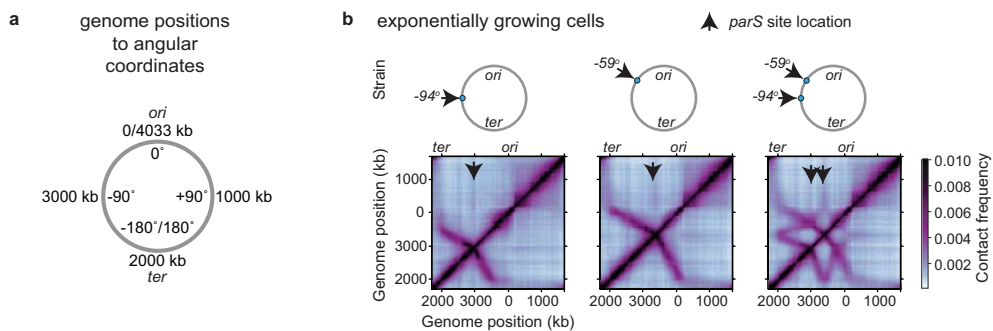
**Extended data** is available for this paper at <https://doi.org/10.1038/s41594-021-00626-1>.

**Supplementary information** The online version contains supplementary material available at <https://doi.org/10.1038/s41594-021-00626-1>.

**Correspondence and requests for materials** should be addressed to L.A.M. or X.W.

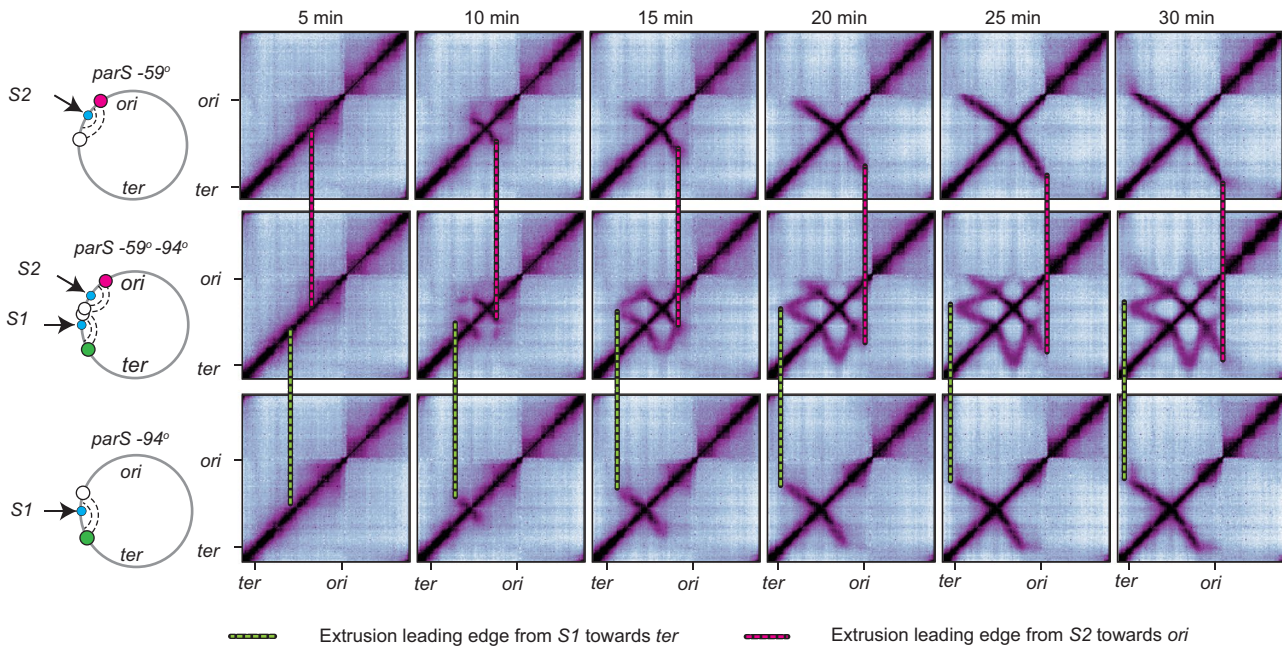
**Peer review information** *Nature Structural & Molecular Biology* thanks Davide Michieletto, Marcelo Nollmann and the other, anonymous, reviewer(s) for their contribution to the peer review of this work.

**Reprints and permissions information** is available at [www.nature.com/reprints](http://www.nature.com/reprints).

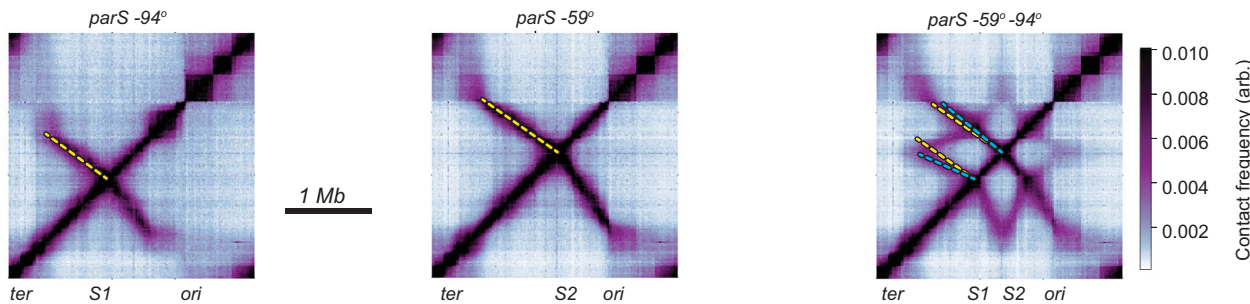


**Extended Data Fig. 1 | Exponential growth does not strongly affect the Hi-C contact patterns.** **a**, The *B. subtilis* genome is displayed in genomic coordinates (kilobases) and the angular coordinates used to designate the locations of the *parS* sites. **b**, Hi-C maps for cells in exponential growth for the strains with *parS* sites at  $-94^\circ$ ,  $-59^\circ$ , and both  $-94^\circ$  and  $-59^\circ$ . For details on strain names refer to Supplementary Table 1 and 2.

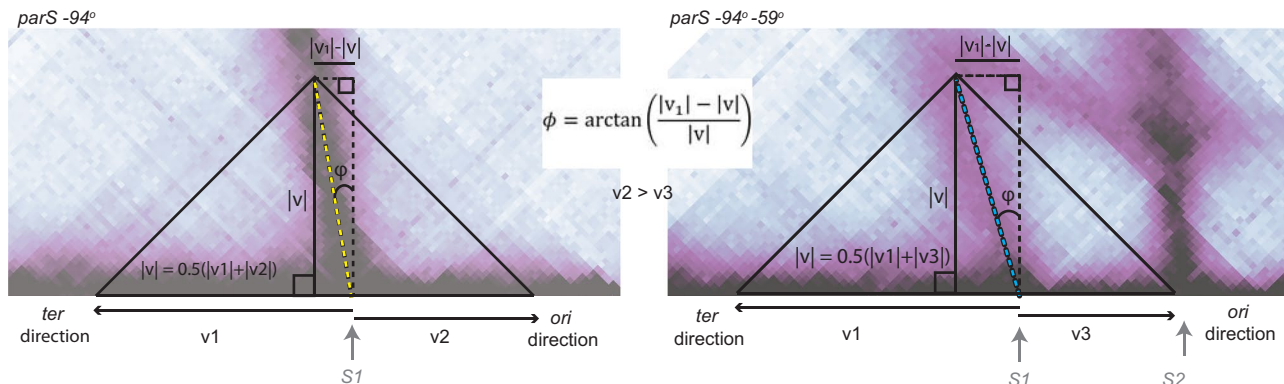
**a** Rates of extrusion away from the S1 and S2 *parS* sites remains the same irrespective of whether 1 or 2 *parS* are present



**b** Extrusion hairpins angle away from each other when there is more than 1 *parS* site

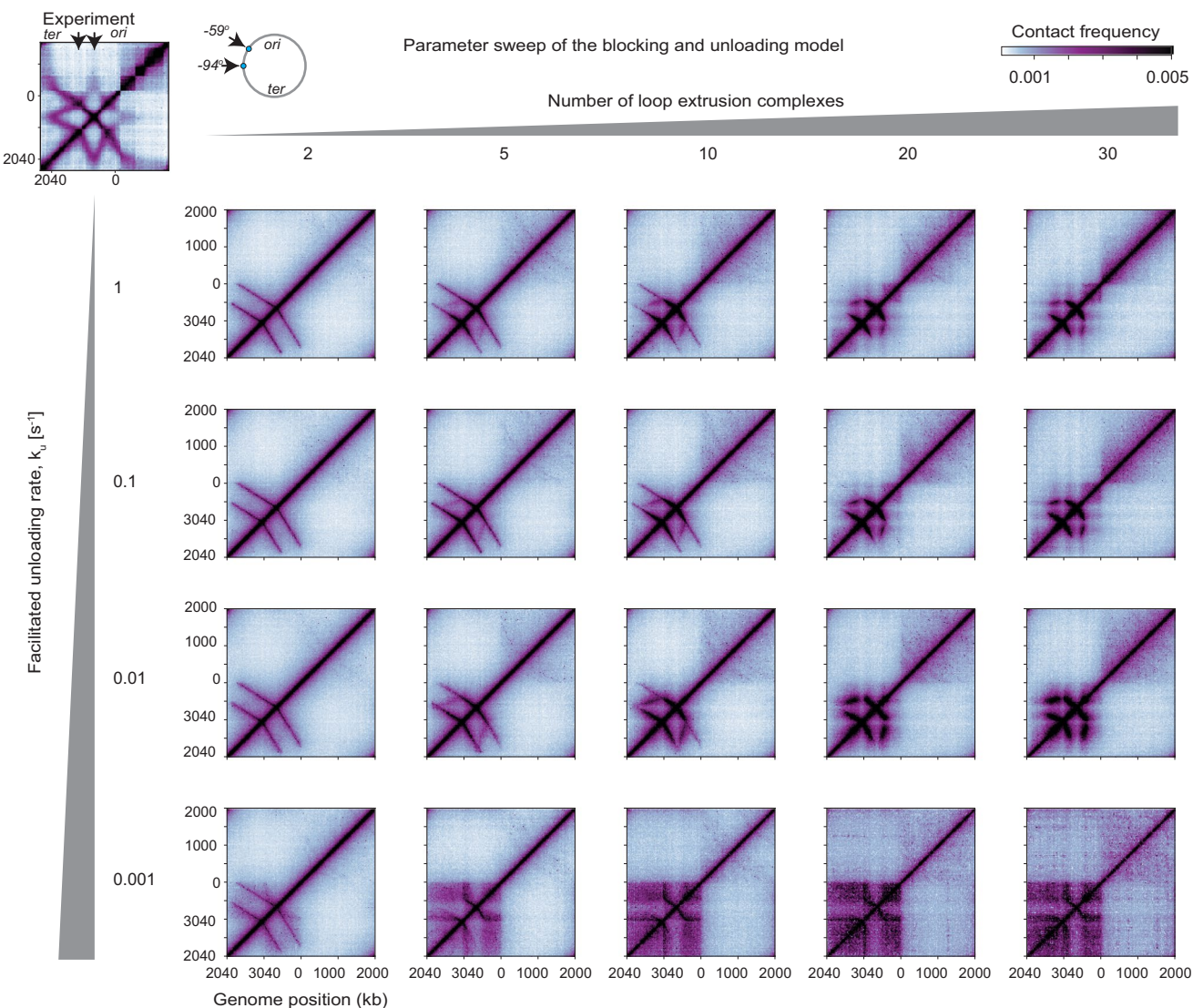


**c** Rates of extrusion between the S1 and S2 *parS* sites is slower when 2 *parS* are present

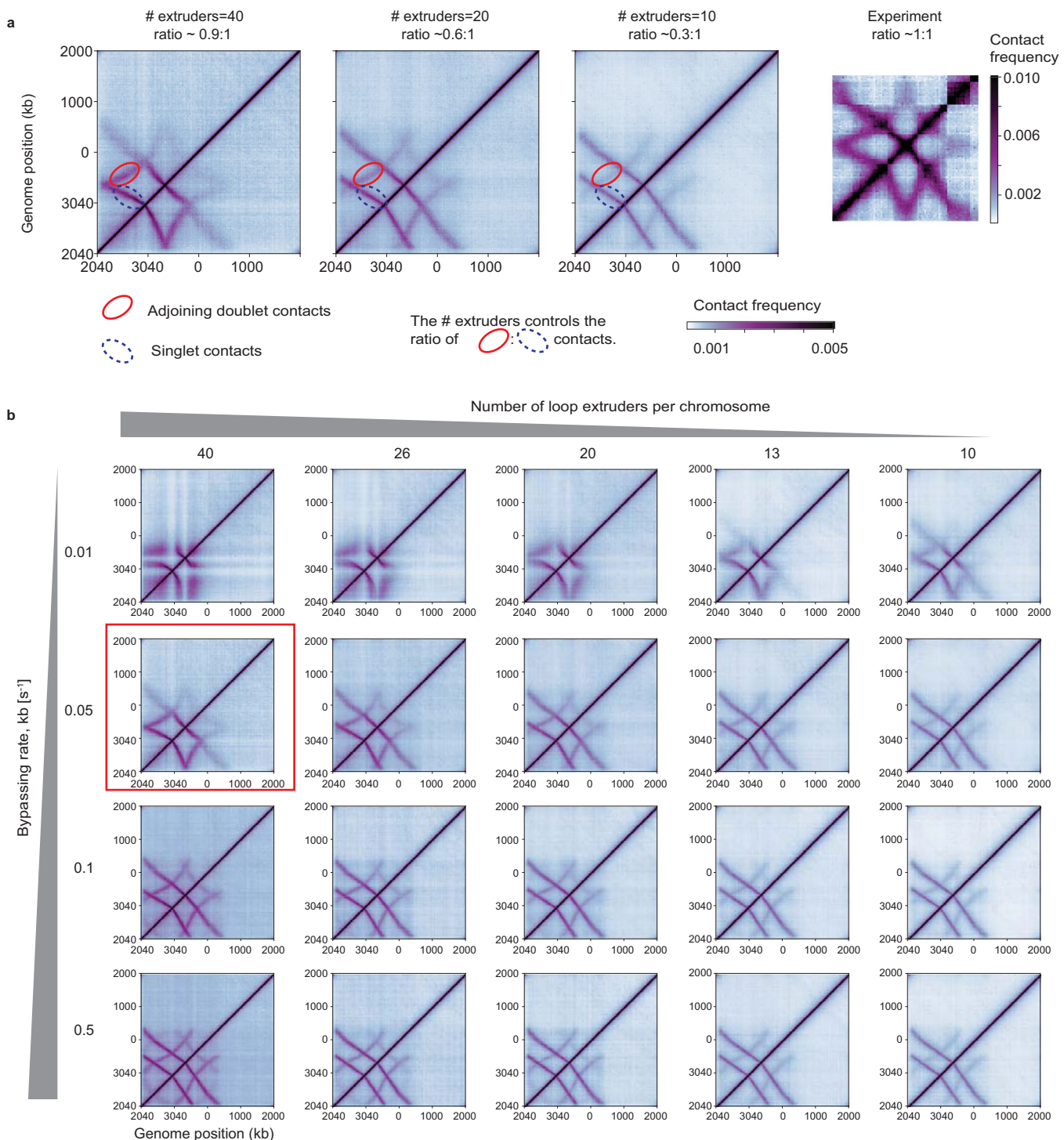


**Extended Data Fig. 2 | SMC complexes can slow each other down.** **a**, Time-course (similar to Fig. 1d) comparing the extrusion rates away from (but not between) the S1 and S2 *parS* sites. The green dashed line tracks the leading edge of the hairpin trace as it emerges from the  $-94^\circ$  *parS* (S1) site and moves towards the *ter*; the red dashed line tracks the leading edge of the hairpin trace as it emerges from the  $-59^\circ$  *parS* (S2) site and moves towards the *ori*.

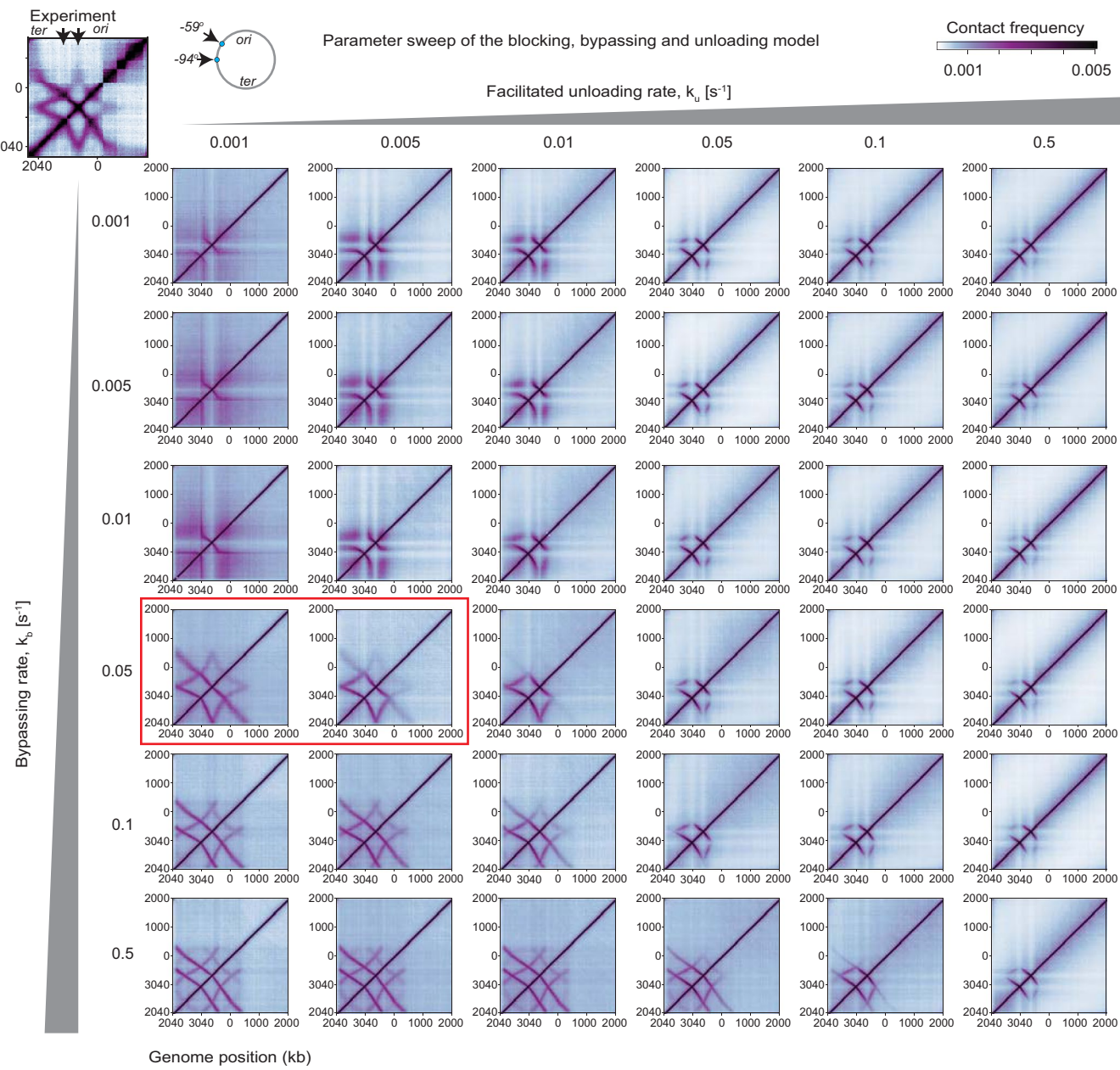
**b**, Demonstration that when two *parS* sites are in one strain, the angle of the hairpin traces changes compared to single *parS* sites. The yellow and blue dashed lines are superimposed on the Hi-C map to help visualize the angle change. **c**, The relationship between the tilt of the hairpin trace and the loop extrusion speeds ( $v_1$ ,  $v_2$  and  $v_3$ ) is captured by a simple geometric relation. The equation shows that for equal  $v_1$  across strains with one or two *parS* sites (as indicated in panel (a)), it follows that  $v_2 > v_3$ .



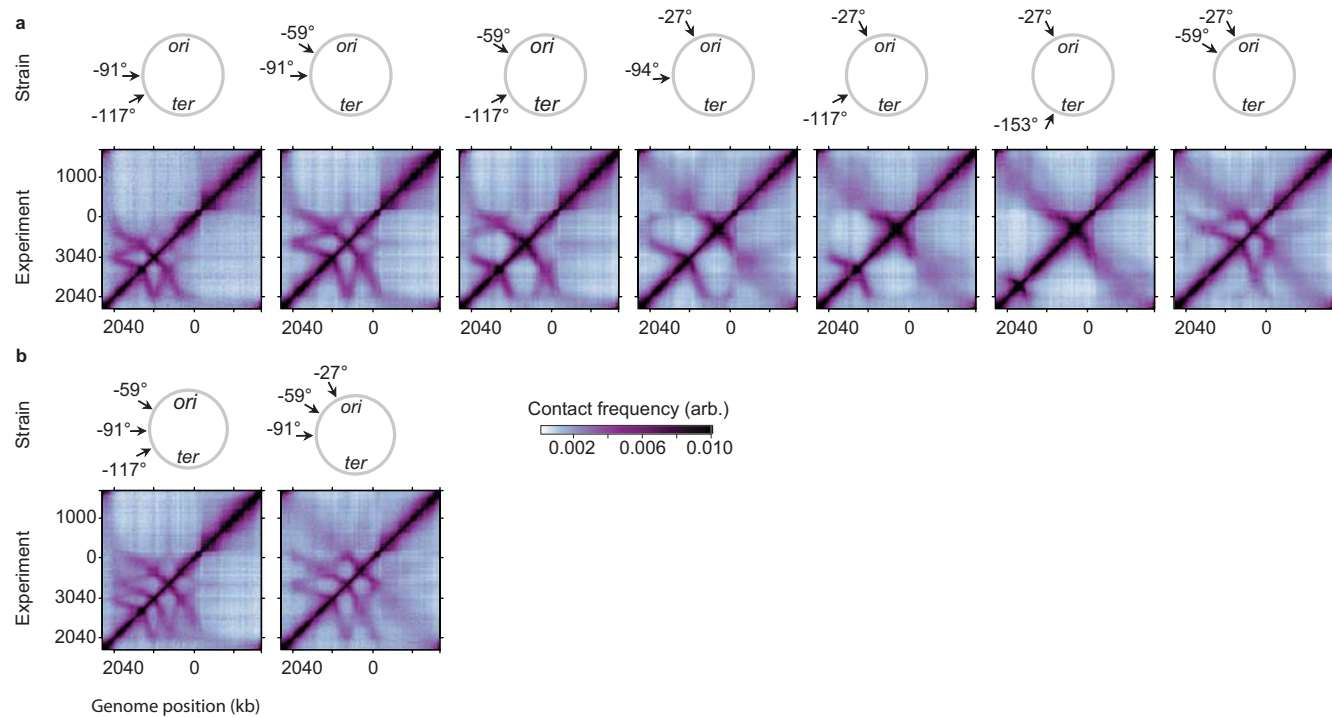
**Extended Data Fig. 3 | The blocking and unloading model of loop extruder interactions does not produce all the features seen in the Hi-C map.** The parameter sweep was conducted for varying numbers of extruders and facilitated dissociation rates. The experimental data (for the strain with *parS* sites at both  $-94^\circ$  and  $-59^\circ$ ) is shown on the top left of the figure. These contact maps were generated with the semi-analytical approach without making the shortest path approximation as described in Appendix 3 of Banigan et al, 2020<sup>30</sup> (also see Supplementary Notes 1-5). Notably, Lines 4 and 5 are missing in all of the plots with the blocking and unloading model - this is due to either traffic jams forming between extruders (for high numbers of extruders), or an insufficient loading rate (for low numbers of extruders) preventing the efficient formation of nested doublets and triplets.



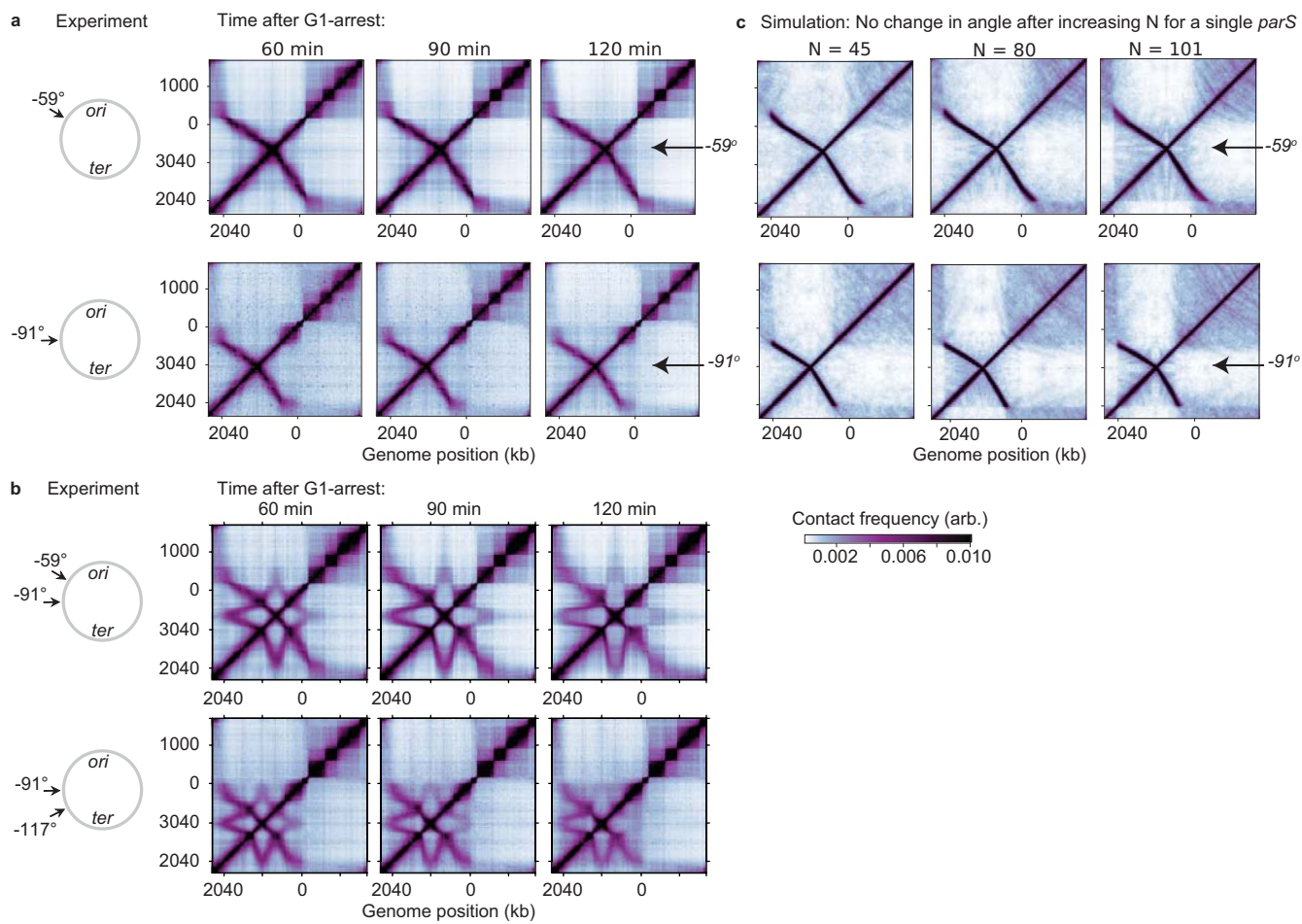
**Extended Data Fig. 4 | The number of extrusion complexes tunes the relative frequency of singlet- to adjoining-doublet interactions.** **a**, In the experimental Hi-C map for the  $-59^\circ$ – $94^\circ$  strain after 60 min of SirA expression, the frequency of singlet contacts to adjoining doublet contacts is close to 1:1. This is only achieved when the number of extrusion complexes is  $>40$  and for sufficiently high bypassing rates. **b**, A parameter sweep over the number of extruders and the bypassing rate. The best matched parameter combination is shown boxed in red. For a description of how we obtained the overall best parameters, see Methods and Supplementary Figs. 4–7.



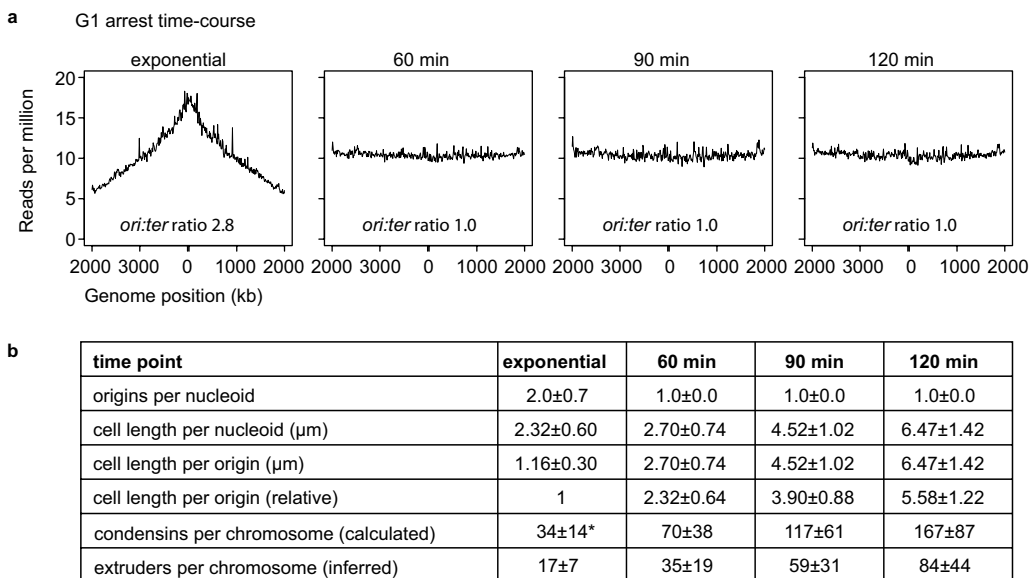
**Extended Data Fig. 5 | Parameter sweep of the bypassing and unloading rates for  $N=40$  extruders/chromosome.** The experimental data (for the  $-59^\circ$ – $-94^\circ$  strain) is shown on the top left of the figure, and the model parameter sweep is below. The model with the most similar pattern in both angles of the Hi-C traces and the relative intensities of the different lines corresponds to a bypassing rate of  $0.05\text{ s}^{-1}$  and an unloading rate between  $0.001\text{ s}^{-1}$  and  $0.005\text{ s}^{-1}$ . From the sweep, we find that the bypassing rate can control the angle between Hi-C map hairpin structures, while the ratio of the bypassing to unloading rates tunes the relative frequency of nested-doublet and nested-triplet interactions. These contact maps were generated with the semi-analytical approach<sup>30</sup> (see Supplementary Notes 1–5).



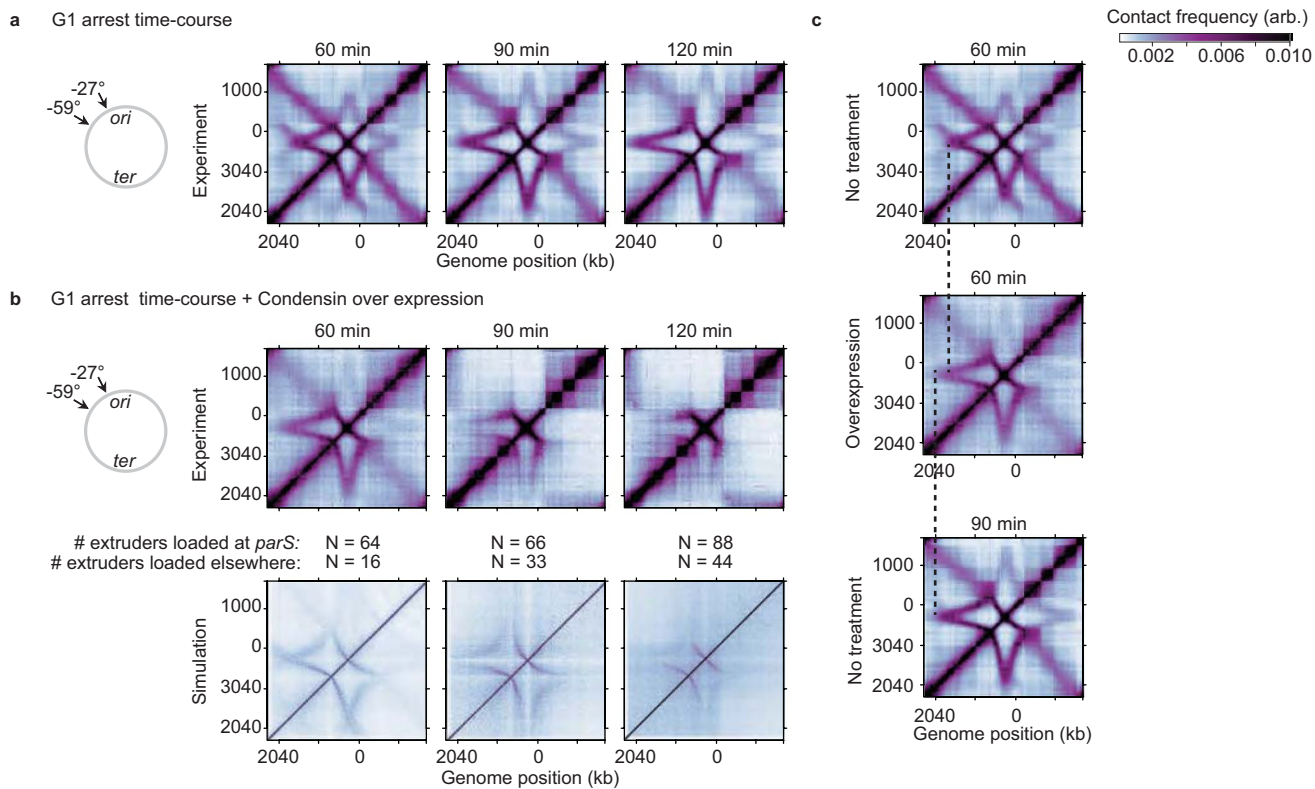
**Extended Data Fig. 6 | Hi-C maps for exponentially growing cells.** Hi-C maps for strains with (a) two *parS* sites, and (b) three *parS* sites. Cells were growing exponentially.



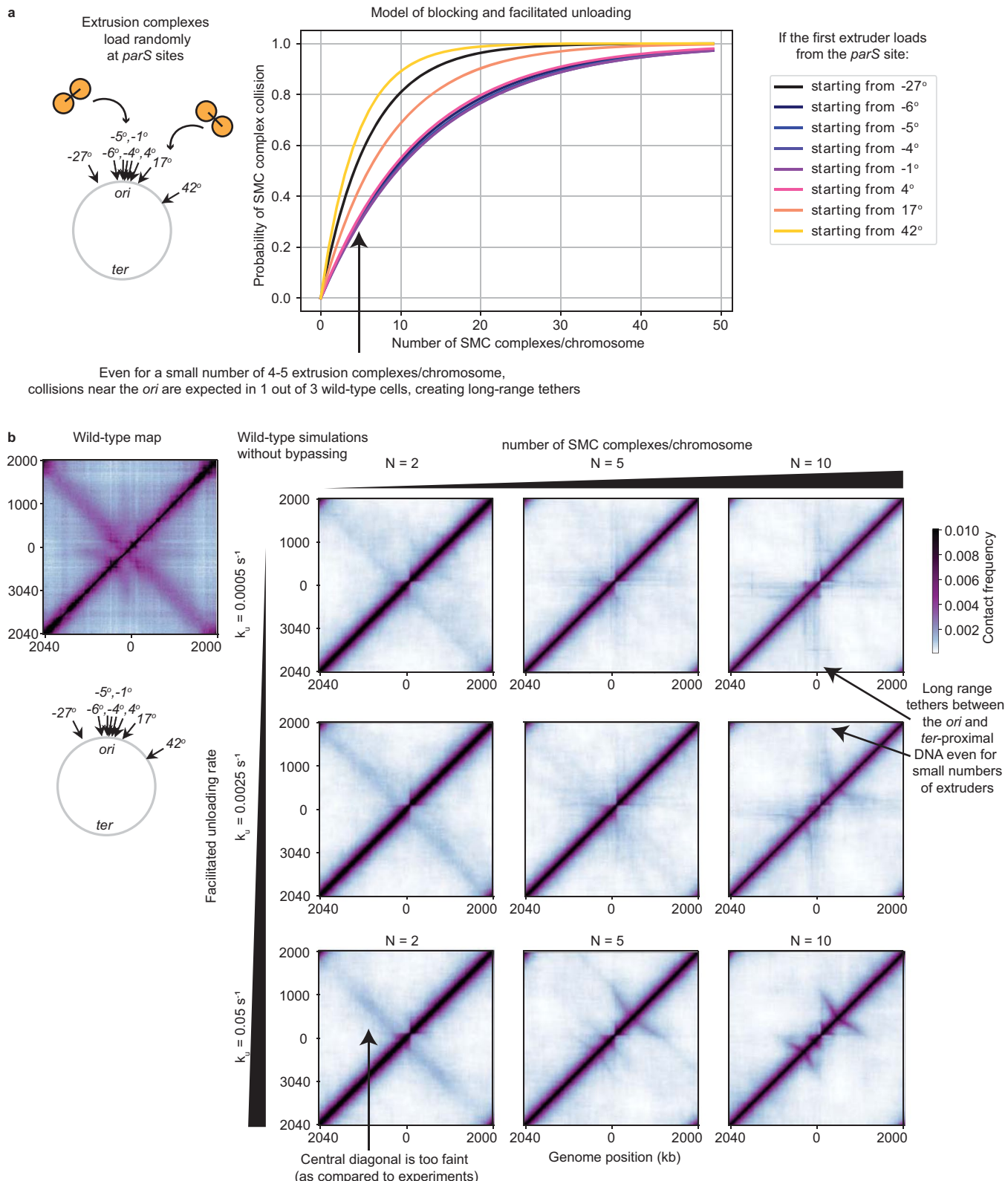
**Extended Data Fig. 7 | Hi-C time course of cells under G1 arrest.** The experimental time course of G1 arrest for a strain with (a) a single *parS* site at the  $-59^\circ$  (top) and  $-91^\circ$  (bottom), and (b) with two *parS* sites at  $-59^\circ$ – $-91^\circ$  (top) and  $-91^\circ$ – $-117^\circ$  (bottom). The experiments show that almost no change occurs to the angle of the hairpin traces when only a single *parS* site is present. However, when two *parS* sites are present, the hairpins increasingly tilt away from each other. c, A 3D polymer simulation with the blocking, bypassing and unloading model of loop extrusion showing that when a single *parS* site is present, increasing the numbers of loop extruders, N, on the chromosome also does not change the observed hairpin angle for the same strains as in (a). Loop extrusion parameters use a bypassing rate of  $0.05\text{ s}^{-1}$  and a facilitated dissociation rate of  $0.003\text{ s}^{-1}$  (that is same as Fig. 4a); the number of extrusion complexes is denoted by N.



**Extended Data Fig. 8 | Quantification of chromosome copy numbers and cell lengths per nucleoid.** **a**, Whole genome sequencing plots for cells after the indicated minutes of replication inhibition by SirA. The computed *ori:ter* ratio indicates that by 60 min of SirA expression, cells have finished chromosome replication. **b**, The quantification of microscopy images reveals the numbers of origins per nucleoid, and cell lengths per nucleoid. The numbers of cells analyzed were  $n=725, 580, 702, 557$  for the four time points (exponential, 60 min, 90 min, 120 min), respectively. Means and standard deviations are shown. These values are used to calculate the numbers of SMC complexes per chromosome at different time points. To estimate the absolute numbers of SMC complexes/chromosome (independently of the Hi-C data and polymer simulations), we use the reference value of 30 SMC complexes/*ori* as measured in (Wilhelm et al, 2015)<sup>32</sup>, which converts to 34 SMC complexes/chromosome (indicated by \*). We infer that these calculated values agree well with the numbers of loop extrusion complexes (as found by Hi-C and polymer modeling), if there are two SMC complexes per loop extrusion complex; this inference assumes that the error on the reference value of 30 SMC complexes/*ori* is sufficiently small. For calculations, see the attached Supplementary Data.



**Extended Data Fig. 9 | Overexpression of SMC complexes speeds up the change of Hi-C patterns with time.** **a**, Replication inhibition Hi-C time course following induction of SirA for a strain with *parS* sites at  $-27^\circ$  and  $-59^\circ$ . **b**, The SMC complex (SMC, ScpA and ScpB) was overexpressed in the same background as the strain in panel A. We found that prolonged over-expression of SMC complexes at 90 min and 120 min did not recapitulate the experiments seen in G1 arrested cells in (a) but caused the interaction lines to become shorter. These patterns are likely due to non-specific loading of SMC complexes outside of *parS*, creating traffic jams along the DNA. In simulations, when we increase the numbers of off-*parS* loaded extruders, while keeping the numbers of on-*parS* loaded extruders consistent, we can observe similar changes in the Hi-C maps. Numbers of on-*parS* versus off-*parS* loading are average values for the simulation. **c**, With SMC overexpression, the 60 min time point (following SirA induction) more closely resembles the 90 min point than the 60 m time point with no SMC overexpression. This indicates that increasing the numbers of SMC complexes on the chromosome leads to an increase in the tilts of the hairpin diagonals away from each other.



**Extended Data Fig. 10 | Simulations of blocking and unloading (without bypassing) do not reproduce the wild-type Hi-C map.** **a**, Analytical results demonstrating there is a high likelihood of collisions between SMC complexes near the *ori* due to the high density of *parS* sites. Calculations were performed for a facilitated unloading rate of  $0.0006 \text{ s}^{-1}$  and an extrusion rate of  $0.8 \text{ kb/s}$ . **b**, 3D polymer simulations showing that even a few loop extruders (for example 5 extruders) results in a missing central diagonal and long-range tethers between the *ori* and other genome positions. With more extruders per chromosome, the traffic jams between SMC complexes near the origin becomes more likely, preventing juxtaposition of the arms. For very low numbers of extruders (for example 2 extruders), the central diagonal is present, but it is much fainter than observed experimentally.